Journal of Volcanology and Geothermal Research 245-246 (2012) 81–97

Contents lists available at SciVerse ScienceDirect

Journal of Volcanology and Geothermal Research

journal homepage: www.elsevier.com/locate/jvolgeores

LiDAR derived morphology of the 1993 Lascar pyroclastic flow deposits, and implication for flow dynamics and rheology

D.E. Jessop [a,b,c,*], K. Kelfoun [a,b,c], P. Labazuy [a,b,c], A. Mangeney [d], O. Roche [a,b,c], J.-L. Tillier [e], M. Trouillet [e], G. Thibault [e]

[a] Laboratoire Magmas et Volcans, Clermont Université, Université Blaise Pascal, Laboratoire Magmas et Volcans, BP 10448, F-63000 Clermont-Ferrand, France
[b] CNRS, UMR 6524, LMV, F-63038 Clermont-Ferrand, France
[c] IRD, R 163, LMV, F-63038 Clermont-Ferrand, France
[d] Institut de Physique du Globe de Paris, Université Paris Diderot 7, PRES Sorbonne Paris Cité, CNRS-UMR 7154, France
[e] Éléctricité de France (EDF), France

ARTICLE INFO

Article history:
Received 19 November 2010
Accepted 30 June 2012
Available online 11 July 2012

Keywords:
Pumice flow deposits
Lascar
Morphology
Dynamics
Kinematics
Velocity
LiDAR

ABSTRACT

Pumice flows are potentially destructive volcanic events that derive from eruption column collapse and whose dynamics are poorly understood. The challenges in studying these flows include the lack of constraints on the dynamics, kinematics and initial conditions that control their emplacement. We present a morphological study of the distal deposits (lobes) of the pumice flows resulting from the 1993 eruption at Lascar, Chile. The surface geometry of the lobes was measured in detail using a LiDAR device, which allowed for detailed characterisation of their morphology, consisting of central channel and lateral levees, and terminal frontal snout. In particular we find that the ratio of channel/levee height as a function of the ratio of the distance between levees/total width of the lobe has a characteristic curve for these pumice flow lobes. Our analysis of several of the Lascar pumice lobe deposits (south east sector) identified several dimensionless groups of the available parameters which, when compared against published results from both experimental and numerical investigations, allowed us to constrain crucial kinematic and dynamic information on the terminal phase of the pumice flows. Notably, we estimate the velocity of the terminal phase of pumice flows to be 5–10 m/s. Froude numbers of 1.5–2 are comparable with values found for experimental granular flows. Height–width aspect ratios for the levee–channel section of the pumice lobes are similar to those for experimental flows although these same aspect ratios for the snout are much larger for the natural deposits than their small-scale analogues. Finally, we discuss the possible emplacement dynamics of the terminal Lascar 1993 pumice flows. A pseudo-Reynolds number based on the velocity estimation is found to be up to 100 times larger for the pumice flows than experimental-scale flows. This suggests that the flow-retarding frictional forces for large-scale flows are relatively unimportant compared to flows at smaller scales. Mechanical effects such as fluidisation, mobilisation of material lying on the slopes over which they propagate and lubrication due to polydispersivity could provide an explanation for their ability to propagate on shallow slopes (6–11°).

1. Introduction

Pyroclastic density currents (PDCs) are among the most hazardous of volcanic processes. One way in which PDCs are formed is through the collapse of eruption columns which occur during explosive volcanic eruptions, generating gravitational flows of gas–particle mixtures that can move at high velocities. The generally accepted conceptual model of a PDC is of a cloud of fine ash particles that often obscures the motion of an underlying dense layer of granular material (i.e. the pyroclastic flow, Cole et al., 1998; Druitt, 1998; Calder et al., 1999). As well as via the collapse of the eruption column, rapid sedimentation of dilute pyroclastic surges can also lead to secondary dense PDCs (Calder et al., 1999; Choux and Druitt, 2002; Druitt et al., 2002; Doyle et al., 2008). In this study we concentrate on the dense, ground-hugging avalanches which are capable of travelling distances of many kilometres. It is believed that the dense basal layer shares many physical similarities with other geophysical flow phenomena such as debris flows as well as rock and snow avalanches, all known to exhibit qualitative behaviour comparable with granular flows (Iverson, 1997; Calder et al., 2000; Kern et al., 2004; Ancey, 2007; Mangeney et al., 2007a, 2010; Mangeney, 2011).

The physical understanding of the dynamics and emplacement processes of PDCs is still an open question, with tremendous implications in terms of risk assessment. The natural complexity of these gravitational flows comes from the wide range of initial and boundary conditions:

* Corresponding author. Tel.: +33 473346793.
E-mail address: d.e.jessop@gmail.com (D.E. Jessop).

0377-0273/$ – see front matter © 2012 Published by Elsevier B.V.
doi:10.1016/j.jvolgeores.2012.06.030

volume, mass flux, grain size, particle concentration, bulk density, topographic constrains (Branney and Kokelaar, 1992; Druitt, 1998) as well as from the different flow regimes from dilute flows, gas-fluidised granular suspensions to dense granular flows where gas plays a subsidiary role (Calder et al., 2000; Roche et al., 2004; Lube et al., 2007). One of the tricky questions is how these flows are able to travel over such large distances over shallow slopes whilst at the same time developing morphological structures (levees, steep fronts, etc.) similar to dry granular flows.

The lack of data on the dynamics of such events prevents quantification of the physical processes at play during flow emplacement. PDCs are destructive, unpredictable events making it difficult to perform measurements of their motion along the slope. For instance, dynamic measurements, such as the stresses and pressures within the flows are up to now impossible for many practical reasons. New research based upon the interpretation of seismic signals generated by geophysical gravitational flows using numerical simulations has allowed the magnitude of basal stresses and flow dynamics to be constrained (Favreau et al., 2010; Hibert et al., 2011). Nevertheless, the vast majority of our understanding of the physical behaviour of PDCs has come from studying their deposits (e.g. Rowley et al., 1981; Wilson and Head, 1981). The internal structure of the deposit has been widely investigated making it possible to show the evidence of segregation processes within a vertical section of the deposit and also laterally (e.g. Lube et al., 2007).

Of particular interest are the data on the detailed morphology of the deposits such as the spatial thickness variations, the shape of the frontal zone and the characteristics of the levee–channel morphology of distal deposits that can be quantitatively compared to the experimental and numerical modelling of granular flows. Indeed, despite the tremendous complexity of natural flows and the resultingly high variability of field data, comparison between observed and experimental or numerical trends through the morphological features or scaling laws provides a means of building and testing hypotheses on the mechanisms at work during emplacement. Whilst similar trends may suggest flow behaviour close to granular flows, differences may highlight the effect of physical processes not accounted for in the existing laboratory or numerical models. The challenge is to compare observations and models given the unknown initial eruption conditions in natural context, possible multiple flow events at the origin of the deposit, the strong heterogeneity of material, particle sizes involved and the unsteadiness of the flow and source, and the variable natural topography whilst existing experiments are almost all performed with simple materials, constant source conditions and slopes (e.g. Pouliquen, 1999b; Roche et al., 2002; Félix and Thomas, 2004; Mangeney et al., 2007b; Jessop, 2009).

Very accurate descriptions of PDC deposits have been provided in the literature (e.g. Sparks, 1976; Branney and Kokelaar, 1992; Sparks et al., 1997; Calder et al., 2000; Lube et al., 2007). In particular, Sparks et al. (1997) and Calder et al. (2000) investigated in detail the spatial distribution of PDC deposits produced by the 1993 eruptions of Lascar Volcano (Chile) and their internal structure. Their work showed evidence of different types of deposit morphologies depending on the distance from the source and on the slope of the volcano. They showed the existence of levee–channel morphologies in the distal part of these deposits (slopes $\simeq 5°$) which have also been observed in other PDCs (e.g. Rowley et al., 1981). Lube et al. (2007) provided a detailed description of the PDC deposits produced by the 1975 Ngauruhoe eruption in New Zealand, reporting distal levee–channel facies on gentle to moderate slopes ($<20°$). These levee–channel morphologies form finger-like lobes exhibiting a bulbous steep frontal snout composed of large particles and, behind, a region exhibiting thicker lateral levees than the central channel. The levees are composed of coarser grains than the thinner central channel. These structures are assumed to be reminiscent of the flow properties (velocity, rheological parameters such as friction and yield stress) during the latest stage of PDC emplacement (Hulme, 1974; Wilson and Head, 1981; Pyle and Elliott, 2006). Even though they only represent a very small part of the deposit (<4% of the total distance from source) and a very short time in the flow dynamics, they may be very useful to understand the capacity of the PDCs to flow over such small slopes.

Our aim here is to provide high resolution measurements of the deposit thickness and morphology of eight individual lobes identified in the distal S–E deposits of Lascar Volcano, related to the eruption which has been described by Smithsonian Institution (1993), Sparks et al. (1997) and Calder et al. (2000). The morphology of some terminal lobes has been measured using a laser scanning device known as LiDAR (Light Detection and Ranging), which provides high spatial resolution data. These data make it possible to investigate scaling laws between the morphometric characteristics of the distal part of the deposits (shape of the front, thickness of the levees and central channel, etc.) and the slope of the topography that are expected to provide good constraints for future numerical modelling and experiments of granular flows designed to understand natural flows. Indeed, Calder et al. (2000) provided indications that terminal lobes of the 1993 Lascar PDCs may behave as dense (dry or fluidised) granular flows. In this work, analyses of these morphological features are performed and compared with published experimental and numerical results on granular flows. Rough estimates of the effective properties of the PDC terminal lobes such as mean friction coefficient, effective viscosity and velocity are provided and hypotheses are proposed to explain the similarities and differences between field observations and experiments.

2. Description of the region studied

Lascar Volcano (northern Chile, 5592 m; 23°22′S, 67°44′W, see Fig. 1a) is located at the western margin of the South American subduction zone in the Central Volcanic Zone (CVZ), the largest active volcanic province in the Andes, on the Altiplano to the east of the Atacama Basin. It is an andesitic-to-dacitic composite stratovolcano, formed by five nested craters oriented in a NE–SW direction (the central crater being the currently active one) and is considered the most active volcano in the CVZ (Francis and Rothery, 1987; Gardeweg et al., 1998). Lascar Volcano has displayed cycles of activity characterised by degassing, lava dome extrusion, pressurisation and explosion during the 1990's (Matthews et al., 1997). Its activity is characterised by persistent fumarolic emissions occasionally interrupted by vulcanian explosions, generating 5–12 km high ash columns.

The largest historically recorded eruption at Lascar occurred on 19–20th April 1993, emitted a total volume of approximately 10^8 m^3 of magma (Pavez et al., 2006) and produced a 25 km high subplinian column. The collapse of the eruption column generated pyroclastic pumice flows that extended up to 8.5 km NW and 4 km SE of the summit (Smithsonian Institution, 1993; Sparks et al., 1997; Calder et al., 2000; Cassidy et al., 2009). The pumice flows spilled over the northern and southern flanks: to the north, the flows were channelised in short sections of their path and spread over ancient lava flows which were highly eroded by their passage (Sparks et al., 1997; Calder et al., 2000); to the south, most of the flows appear to have followed a gully (label A in Fig. 1b) until its end (B) whereupon they spread out over a plain (see Fig. 10 of Calder et al., 2000, and Fig. 1b). There were a number of explosive events which generated pyroclastic flows, particularly on the 19th April (Smithsonian Institution, 1993), and see Table 1 of Cassidy et al. (2009). This resulted in a deposit which is composed of the products of several different flow units (Sparks et al., 1997; Calder et al., 2000; Cassidy et al., 2009). This deposit is particularly well preserved because the Atacama Basin receives very little precipitation that might alter or obscure it. There has been no important volcanic activity since the 1993 eruptions so the deposits today are very well preserved and in much the same condition as shortly after the eruption in 1993. Minor compaction attributed to regional earthquakes, however, has been reported by Whelley et al. (2011).

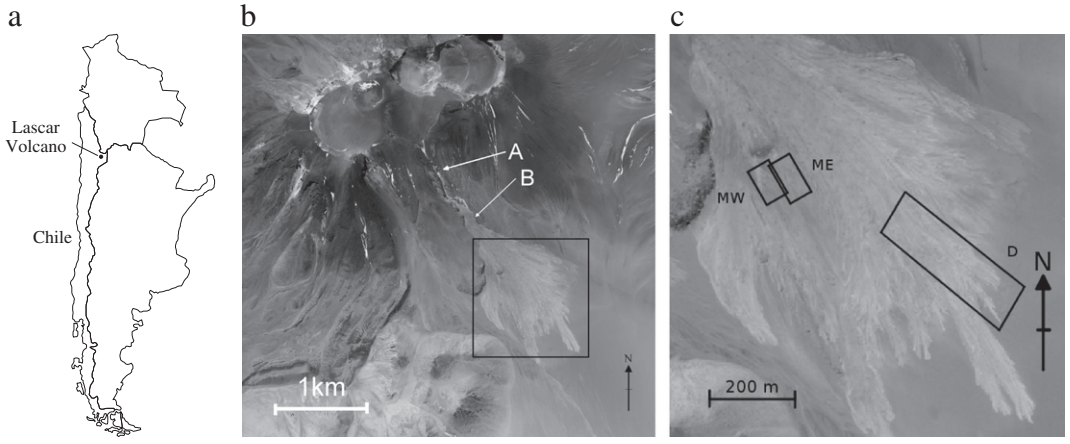

Fig. 1. (a) Location of Lascar Volcano, Chile. (b) Aerial photograph of Lascar Volcano and the area to the south east which was inundated by pumice flows during the 1993 eruption and (c) a zoomed-in view highlighting the medial (MW, ME) and distal (D) sectors that were studied. The labels in (b) correspond to: A) the gully feature through which the pyroclastic flows were initially channelled; B) the end of the gully, at which point the flows spread out over a plain of a lower slope angle.

We chose two principal areas of interest from the 1993 pumice flows in the south-eastern sector, one medial and the other distal, which are indicated in Fig. 1c. Slope angles are about 12–18° and 6–10° in the medial and distal sectors, respectively. In the medial sector the flows overrode recently emplaced deposits from the same 1993 event whereas, distally, they were emplaced over an older coarse tephra substrate. We split (arbitrarily) the medial sector into west and east sub-sectors, denoted as MW and ME respectively in Figs. 1 and 2. We chose to focus our analysis on eight individual pumice flow lobes, referred to hereafter by a single numeral between 1 and 8 according to the definitions in the DEMs of Fig. 2. It is important to note that we considered only the most distal part, typically 35–100 m long, of these lobes whose overall length was about 3–4 km. We acknowledge that this represents a small portion of the entire flow length (<4%) so that our analyses are likely to give insights into the flow dynamics only for these restricted areas and at late stages of emplacement. The general form of the distal part of these lobes is a flat channel bordered by lateral levees and which terminates by a rounded snout at the front. Much of the surface of the lobes is composed of large (typically 5–30 cm) pumices as evidenced by Fig. 3 although the interior also contains coarse ashes (Fig. 3c). It is possible that the high winds often encountered here may have elutriated away the finer material of the surface. These pumices are present in higher proportion at the top, base and lateral margins of the lobes, and towards the frontal snout (see Fig. 3a), as reported for other types of coarse-grained pyroclastic flow deposits such as the detailed description at Ngauruhoe in Lube et al. (2007).

3. Methodology

3.1. Surface data acquisition using laser surface scanning

Laser surface scanning works on the principle of measuring the time delay between emission and reception of a pulse of laser light reflected from the target object. It has a history going back several decades, to the 1970s in the case of airborne scanning (Ackermann, 1999) and is commonly used to differentiate land resource usage, such as for building

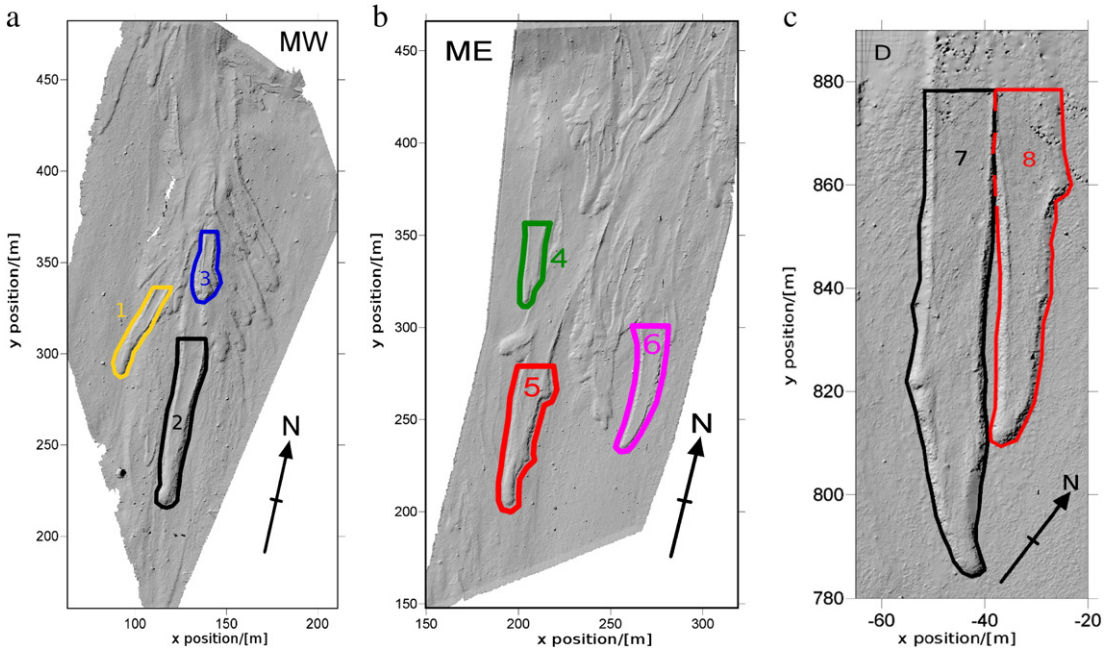

Fig. 2. DEMs for each of the regions of study: (a) west part of the medial sector (MW); (b) east part of the medial sector (ME); (c) distal sector (D). The slope angles are in the range 12–18° in the former two sectors compared to 6–10° for the latter. The coordinate systems for the medial and the distal sectors are with reference to a local datum set arbitrarily during the measurement process.

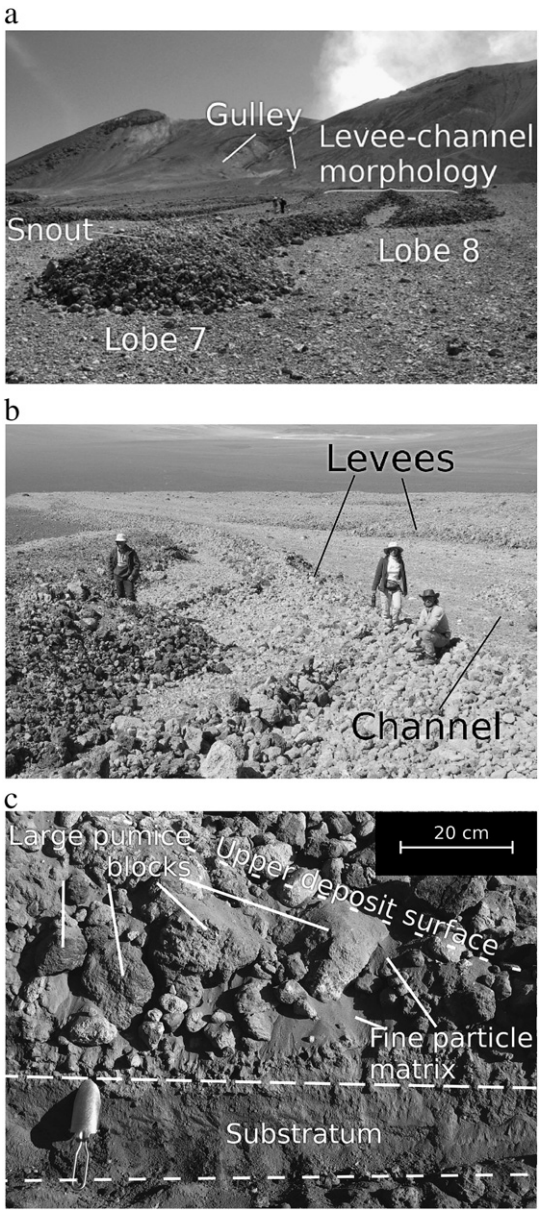

Fig. 3. Pumice flow lobes from Lascar. (a) View of the distal sector of the Lascar deposits (lobes 7 and 8.) The rounded lobe snout recedes into the levee–channel formation further upslope. The gulley (feature A of Fig. 1) can be seen in the far distance. (b) A lobe in the same sector viewed from upstream illustrating more clearly the formation of the levees and the channelised material between them. (c) Interior of a pumice flow lobe showing the mix of fine material and blocks in the interior and surface composed mainly of large pumices.

and agriculture (Ma, 2005). It is only fairly recently, however, that terrestrial scanning has been applied to the production of digital elevation or outcrop models (Bellian et al., 2005; James et al., 2009; Jones et al., 2009) despite this being a purpose to which it is ideally suited. LiDAR (Light Detection And Ranging) has several advantages over traditional methods of three-dimensional terrain mapping, e.g. stereo-photogrammetry, which include very high precision, high degree of automation and immediate recording of data points in Cartesian coordinate system (Baltsavias, 1999). Some disadvantages include the high cost of hardware, necessity for dedicated software and relatively long acquisition times.

We mapped the Lascar pumice flow lobes in 2007 using a terrestrial LiDAR scanner (Riegl LMS-Z420i) provided by the Research and Development group of EDF (Électricité de France), in collaboration with whom this work has been carried out. The Riegl LMS Z420i, has a maximum range of about 800 m. A tripod was used to mount the scanner at a height of approximately 2 m. However, the nature of the terrain meant that there were no natural vantage points from which it was possible to look down upon the lobes. Thus the use of a single scanning station would result in a LiDAR shadow when an object is raised above its surroundings. This phenomenon was remedied by scanning from several locations and combining the data sets (Bellian et al., 2005). The locations of each of the measuring stations were determined by triangulation using differential GPS, distance metre and theodolite. These locations were combined with the data set of each scanning station to create a coordinate system relative to a local datum (see axes of Fig. 2 for example).

3.2. Initial surface estimation

The LiDAR scans measure the topography of the flow lobes, as shown by the DEMs of Fig. 2 which were interpolated from the LiDAR data using an inverse-distance weighted method. In order to study the lobe shape, however, the lobe topography must be separated from the topography of its substrate. This situation is complicated by the fact that many of the lobes are emplaced on top of previous lobes from the same eruptive event, and may have remobilised much of the underlying material (Sparks et al., 1997; Calder et al., 2000).

The process of estimating the initial surface is illustrated in Fig. 4. Initially, a boundary (in the *xy* plane) around each lobe was defined via a polygon (Fig. 4a) and the LiDAR data points lying within the boundary determined using an algorithm based on the Jordan curve theorem. This simply states that from a point lying within a closed curve, such as a polygon, the boundary must be crossed an odd number of times in order to be outside the curve. The ensemble of data outside the polygon was then interpolated to provide an estimation of the pre-emplacement substratum (Fig. 4b). When the substratum estimate is subtracted from the data set only the lobe surfaces remain, as shown in Fig. 4c and d.

3.3. Parameter extraction

The parameters which are needed to quantitatively describe the pumice flow lobes are defined as per Fig. 5: the total width of the lobe, W; the separation of the levees, w; the estimations of the lobe thickness of the lobe at the left, h_l, and right, h_r, levee peaks, and the estimated thickness of the channel h_c. Each of these parameters is recorded as a function of the distance along the axis from the tip, s, and the local slope angle, θ, which is defined below. Also recorded is the length of the lobe snout, L. It should be noted that widths are preserved during this process.

To obtain all of these parameters, thickness profiles such as those illustrated in Fig. 4d are analysed. We wished to have the maximum amount of information from each lobe so we developed an automated data extraction methodology. This allowed us to process a large number (up to 500) of height profiles for each lobe which would have been impractical to do using standard GUI based software. The thickness profiles and parameters were calculated as follows:

1) The approximate positions of the levees were found as the maxima of the interpolated data by scanning along the rows of the matrix of thickness for each lobe.
2) The axis (x_c, y_c) of the lobe (– in Fig. 5a) was defined as the average of these positions. (x_c, y_c) is also the central point of the height profiles.
3) The data points lying adjacent to a line perpendicular to the axis at each (x_c, y_c), within a band of ± 1 m, were then re-interpolated to produce a height profile. The thickness profile is a function of both x and y but can be reduced to a function of a single coordinate, ξ, by writing

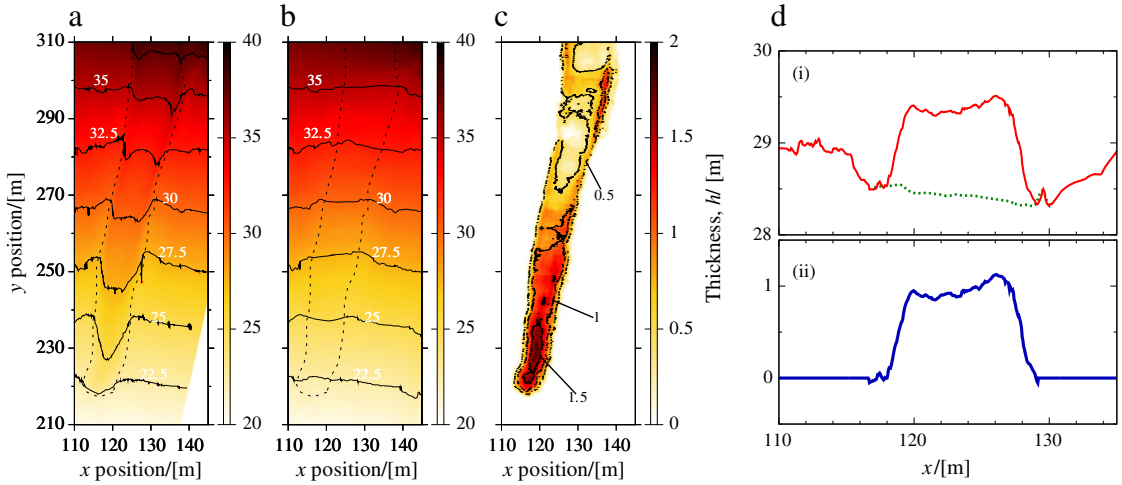

Fig. 4. Relief images illustrating the process of removing the initial slope with the thickness shown with a shaded scale and isocontours (in m). The lobe boundary is illustrated by the dashed (– –) curve. Initial surface data (a). Estimation of the background (b). Subtraction of the surface estimation from the original data revealing the lobe (c). Thickness profiles at $y=260$ m (d): (i) the surface estimation (•••) is subtracted from the initial profile (–) resulting in (ii) the lobe being isolated (–). Note that the vertical scale is greatly exaggerated (1:10) in these images. (For interpretation of the references to colour in this figure legend, the reader is referred to the web version of this article.)

$$\xi = \mathrm{sgn}(x-x_c)\sqrt{(x-x_c)^2+(y-y_c)^2}, \tag{1}$$

where sgn is the signum (sign) function. This coordinate system is redefined for each cross section.

4) The levees are the maximum values of the thickness profile to the left and right of the central point (□ and ○ in Fig. 5a). h_l and h_r are estimated as the value of the height profile at these points, and the separation of the levees, w, is the distance between these two points. The outer edges of the lobes are the points where the thickness became zero and the total width, W, is the distance between them.
5) The slope of the levee flanks, ϕ_{levee} (see Fig. 5b), is approximated by

$$\tan\phi_{\mathrm{levee}} = h_{\mathrm{ave}}/\left(\tfrac{1}{2}(W-w)\right). \tag{2}$$

6) For each lobe, the length of the snout, L, is estimated manually (see Fig. 8).

3.4. Calculating slope angles

The slope angles beneath each lobe were found by fitting the second order polynomial to the elevation of the points (x_c,y_c) on the estimation of the substratum, e.g. Fig. 4b. The polynomial is defined by

$$\theta = a_0 + a_1 s + a_2 s^2, \tag{3}$$

where s is the distance measured from the snout of the lobe and $a_{0,1,2}$ are coefficients determined by linear least squares regression (e.g. Fox, 1997). The estimated slope angles as a function of the distance from the snout are discussed in the following section. The value of $|a_1 s|$ was larger than $|a_2 s^2|$ in all cases sometimes by as much as an order of magnitude so that, in general, the slope angle varies linearly with s.

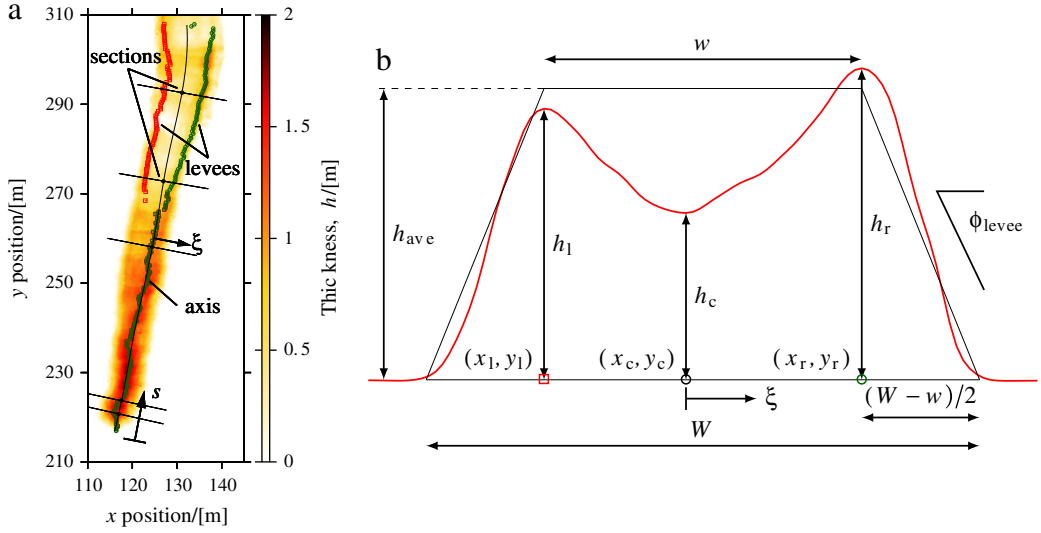

Fig. 5. Definitions and parameters. (a) The isolated lobe from Fig. 2 showing the central axis, the left (□) and right-hand levees (○), the perpendicular sections, the distance from the snout tip, s, and the cross-sectional coordinate, ξ. (b) An example of a cross-sectional height profile of a lobe, such as would be seen in (a). The positions where the lobe thickness at the channel and the left and right levees are measured are given by □ : (x_l,y_l), ○: (x_c,y_c) and ○ : (x_r,y_r) respectively. The approximate angle of the levee flanks, ϕ_{levee}, is calculated from $h_{ave} = \tfrac{1}{2}(h_l+h_r)$, W, and w. (For interpretation of the references to colour in this figure legend, the reader is referred to the web version of this article.)

3.5. Error estimation

There are essentially two sources of error in our analyses: the initial measurement error from the LiDAR scanning and the interpolation error. Beyond this, our measurements are accurate to machine precision. The measurement accuracy of the LiDAR device (Riegl LMS-Z420i) is typically 1 cm at a distance of 500 m. As the pumice flow lobes have features in the order of metres, this relates to about 1% of the thickness. As part of the interpolation the standard error on the vertical elevation was calculated, having a typical value of ± 0.02 m which is equivalent to about 2% of the thickness of the lobes. Overall, therefore, the DEMs produced such as those shown in Fig. 2 have an error of only a few percent.

4. Results

Of the eight lobes chosen from the LiDAR data, lobes 2 and 5 are particularly well defined in that they are relatively straight and lie on slopes which do not vary significantly. Lobes 7 and 8 are also interesting because they appear to be the result of bifurcation of the same upslope surge flow as discussed here. These will be used preferentially when the dynamical and frictional properties of the flow will be estimated from existing results on granular flows over sloping beds.

Fig. 6 shows the evolution of the morphology of lobe 5, including an area upslope not included elsewhere in our analyses (sections 1–4). Here, the substratum has not been removed, as will be done later, so that the interactions between the pumice lobe and its surroundings can be seen clearly. In sections 1, 2 and 4 we had to estimate part or all of the interface between the pumice lobe and the substratum as the complexity of the surroundings (e.g. overlapping lobes, intersections and uneven terrain) made the estimations of the substratum by interpolation unreliable. However, the quantitative analyses we perform were limited to below section 4 so this has no effect on any of the results we present elsewhere. In Fig. 6 we see a well-defined levee–channel morphology (1) transform into the rounded morphology of the snout (9) with bifurcations producing secondary lobes in between (4, 5 and possibly 8). We also see clearly the flank angles which are in the region of 20–30° for the exterior angles and slightly shallower (15–20°) for the interior angles.

It can be seen in section 1 that the right-hand levee (with respect to the image) is much taller than that on the left-hand side and that the underlying substratum is more elevated to the right. The corresponding part of the DEM shows that the flow bends to the left. This asymmetry may be due to the surface of the flow tilting towards the centre of curvature of the bend as a result of the radial acceleration of the lobe and the flowing material "sloshing" towards the outside (see Fig. 14 of Mangold et al., 2010 for an illustration). Consequently, lobe deposit shows larger and broader levees on the outside of the channel bend. This effect and its consequences for flow dynamics will be discussed in more detail in later sections.

4.1. Slope

An approximation to the slope of the substratum as a function of s for the eight lobes, calculated via Eq. (3), is shown in Fig. 7. The distal sector is generally lower in slope than the medial sector with the slope angles in agreement with the field observations stated in Section 3. The slope varies between 6 and 11° for all the lobes. The maximum slope variation along a single lobe is 4° (lobe 7) whereas the slope is almost constant (±1°) for lobes 1, 3, 4, and 5. Generally, the slope angles vary little for the majority of the length of the lobes becoming gentler close to the snout. Exceptions are lobes 3 (▲) for which the slope angle decreases by about 1° over 40 m, 5 (△) which decreases by 1° over 80 m and lobe 6 (●) which increases by less than 1° in the 10 m before the front. As the variation in slope angle is roughly linear and positively correlated with the distance from the front s, the latter parameter can be thought of as showing the global trend of the slope angle. Note that lobe 7 is the best of an approximately linear increase of the slope from the snout to the upper part, with the strongest slope variation. As such, it is a good candidate for estimating the variation of the morphological parameters as a function of slope.

4.2. Longitudinal variations in thickness

In Fig. 8 we show the longitudinal profiles of the pumice flow lobes. For each lobe, three curves are plotted: the thickness along the middle of the central channel h_c, and the thickness along both the right h_r and of the left h_l levees, going from the front to the upslope part of the lobe. Along the bulbous snout, of length L, there is no difference between the profiles and the greatest thicknesses are observed. Further from the front the levees begin to form and, further still, the levee–channel morphology is fully developed until the end of the measured region upslope. The transition zone is defined as being after the snout but before the central channel becomes clearly lower than the two bordering levees.

These three zones (snout, transitional, levee–channel) are qualitatively observed for all the lobes studied. For lobe 1, after the transition zone, the thickness deposit is very small (≃0.1 m) and almost no levees are observed ($h_c \approx h_{ave}$). Due to a lack of LiDAR data in certain areas of the regions studied, we have had to estimate the fronts of lobes 3, 4 and 6. Except for these 3 lobes, the extension of the snout is about the same for the median sector ($25 < L \lesssim 30$ m on slopes 8–10°), whilst it is much shorter in the distal region ($5 < L \lesssim 10$ m on slopes 6–7°). Except for lobe 1 where it is difficult to define, the extension of the transition zone is 6–25 m in the median sector and 2–3 m in the distal region. In the medial sector, h_c for the levee–channel zone does not vary much, except for lobes 3 and 5 where it decreases significantly when going upslope (from 1 m to 0.1 m for lobe 5) on almost constant slopes. In the distal region, for lobes 7(▽) and 8 (▼), h_c decreases upslope as the slope increases and then increases again on the final 20–30 m. In fact, these two lobes probably originate from the same flow pulse which bifurcated forming two separate pumice flow lobes (see Fig. 2c).

Both Sparks et al. (1997) and Calder et al. (2000) reported that the distal pumice flow fans at Lascar often consisted of overlapping lobes. Fig. 8e (lobe 5) in particular shows a distinct and significant secondary hump about halfway along the snout which may be evidence of overlapping. Lobes 1 and 2 (Fig. 8a and b respectively) may also show secondary (and possibly tertiary) humps, although these are much smaller in amplitude. However, we have not been able to determine with any certainty from either the plots shown in Fig. 8, the DEMs (Fig. 2) or photographs taken during the field campaign whether these are indeed cases of separate, overlapping lobes or just unusually shaped individual lobes (e.g. due to fluctuations in the flux).

4.3. Lateral thickness profiles and width variations

The snout and the levee–channel zones can be clearly observed on the cross sections of the lobes (Fig. 9): the tall, rounded shape of the snout is progressively replaced by the levee–channel morphology when moving rearward. The width of the lobe increases from the snout up to the levee–channel zone where it remains roughly constant. Except very close to the front (e.g. $s = 2$ m for lobe 2), the slope of the lateral flanks of the lobe does not vary significantly along their length, ranging from 15 to 20°, excepting the left flank at $s = 75$ m in lobe 5 which is slightly steeper. Furthermore, the slope of the interior of the levees is approximately constant at around 15°.

In Fig. 10a and b the variation of the widths of the lobes is shown as a function of s. Fig. 10a shows that the width between the levees, w, increases as s increases. The total width, W, in Fig. 10b follows a similar

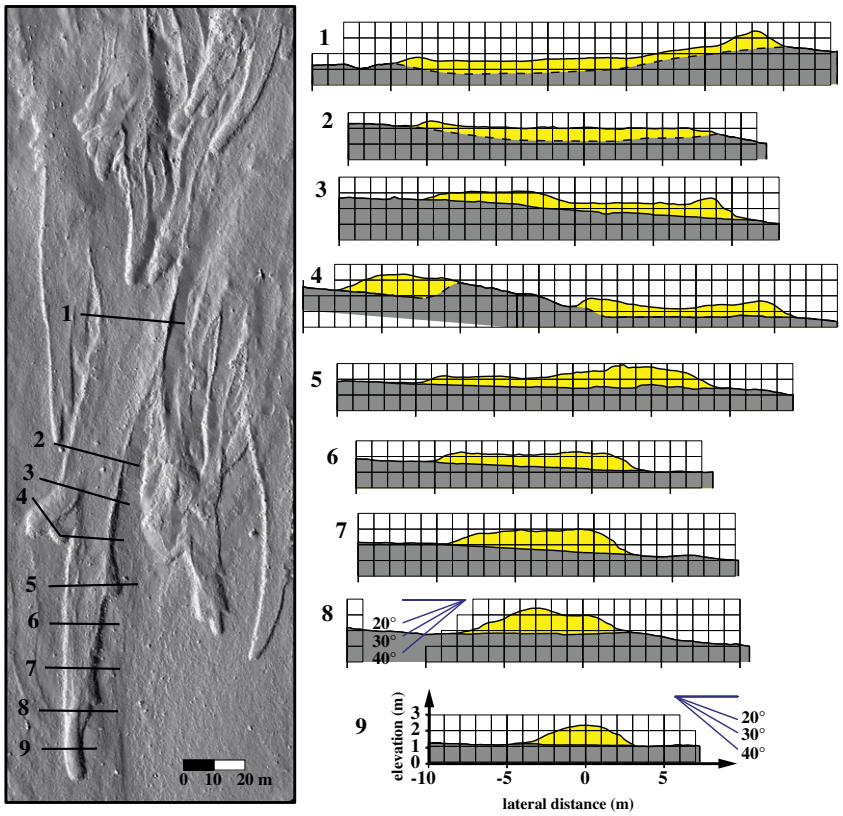

Fig. 6. Enlarged view of part of the DEM for the medial-east sector (area surrounding lobe 5) before any attempts have been made to remove the substratum. Plotted also are nine cross-sectional profiles at various points along the length of lobe 5. These clearly show the variation of the deposit morphology from levee–channel (1) to the rounded snout (9). The substratum (grey) has been identified using the methods described in Section 3 and so the remaining profile is that of the pumice lobe (yellow). The dashed lines marking the interface for sections 1, 2 and 4 are our interpretations of the substratum. (For interpretation of the references to colour in this figure legend, the reader is referred to the web version of this article.)

trend, although less well defined. There is a large degree of variation in the data, especially for lobe 1 in the levee–channel zone. It has already been seen, however, that the levees are very poorly pronounced on this lobe. Lobe 2 shows an almost linear increase of w with s. Although less well defined, linear increases are observed for the other lobes with a gradient that appears to be the same for all lobes.

4.4. Groupings and correlation of parameters

We now attempt to identify well-correlated parameters and dimensionless parameter groups, which may later be useful for comparing the pumice flow lobes to experimental data and numerical simulations. In Fig. 11a, the mean thickness of the levees, $h_{ave} = ½ (h_l + h_r)$, is represented as a function of the thickness of the central channel. All points corresponding to the lobe snout (i.e. where $h_c = h_{ave}$) were removed from the data set before plotting. These two parameters are well correlated with a mean correlation coefficient of 0.86, i.e. h_{ave} increases almost linearly with h_c.

In Fig. 11b the width of the levees, w, is presented as a function of the total width, W. These two parameters are reasonably well correlated with a mean correlation coefficient of 0.72, so W and w increase in a quasi-linear relationship. As an example, W/w varies from 1.7 to 2 in the levee–channel zone for lobe 2. As both Fig. 11c and d illustrate, there is no clear correlation between the thickness of the central channel h_c and the widths W or w. The same is observed for h_{ave} as a function of w and W.

Fig. 11e shows that the difference in total width of the lobe and the levee separation, $W - w$, is roughly correlated with the average levee thickness h_{ave} (mean correlation coefficient of 0.70). A linear fit of this data gives $W - w = (4.86 \pm 0.40) h_{ave} + (2.10 \pm 0.49)$. Using Eq. (2), gives an estimation of the flank angles to be $\overline{\phi}_{levee} = [23.13° \; 26.84°]$. This is in agreement with the slope-angle indicators of Fig. 9 (15–25°). It is interesting to note that the correlation of $W - w$ and h_{ave} holds regardless of the distance from the front s, as indicated by the tone of the data points.

Fig. 11f shows the dimensionless ratios h_c/h_{ave} as a function of w/W. All the data points collapse approximately onto a single curve. The ratio h_c/h_{ave} is obviously equal to 1 along the snout and suddenly decreases around $w/W = 0.4$, which is indicative of the transition between the levee–channel and the snout zones. Far from the front,

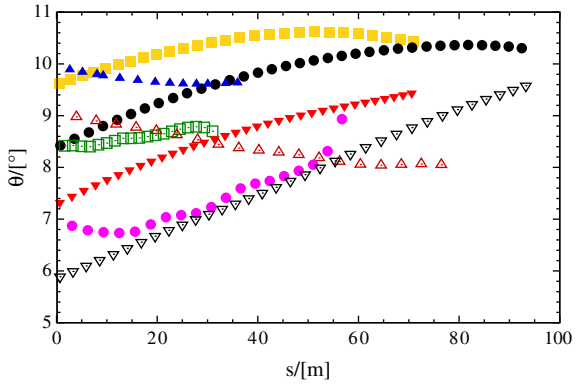

Fig. 7. Mean slope angle, θ, along the length of the lobes (measured from the front), s. The symbols used in this figure correspond to the following sectors and lobes: (median-west) 1 (■), 2 (●), 3 (▲); (median-east) 4 (□), 5 (△), 6 (●); (distal) 7 (▽), 8 (▼). The slope angles calculated agree with field observations, as mentioned in Section 3. (For interpretation of the references to colour in this figure legend, the reader is referred to the web version of this article.)

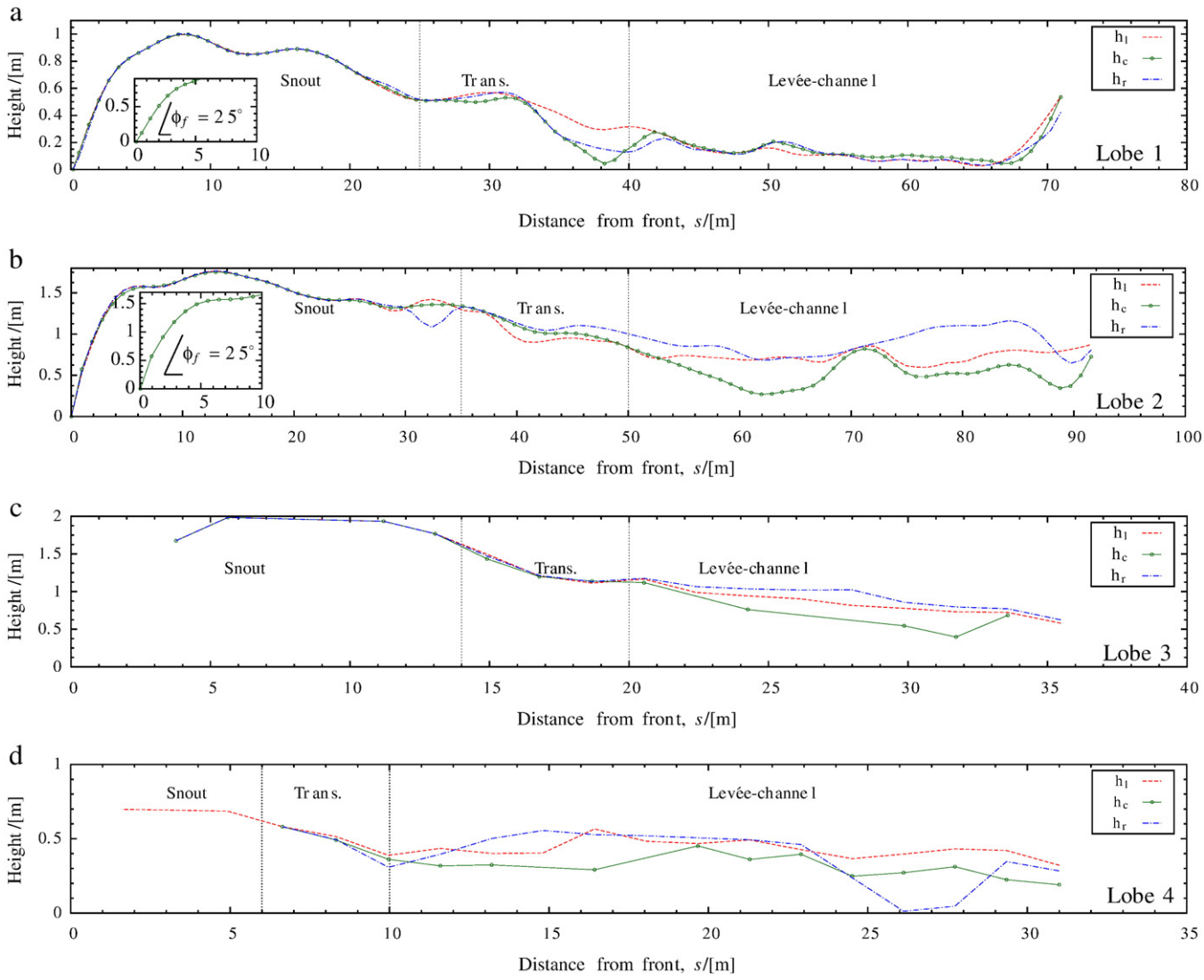

Fig. 8. Longitudinal height profiles along the levees (h_l, h_r) and axis (h_c) of lobes 1 (a), 2 (b) and 3 (c) (medial-west sector) and lobe 4 (d) (medial-east sector). Where the LiDAR coverage was sufficient, we have plotted the points closest to the front (inset) which have slopes close to 25°. Elsewhere the approximate form of the snout has been indicated by a dotted line (...). Also indicated are the approximate regions of different morphologies: the snout and an estimation of its length, L, transition, and fully-developed levee–channel form. (For interpretation of the references to colour in this figure legend, the reader is referred to the web version of this article.)

many data points clustered around the value $h_c/h_{ave} = 0.5$. We believe that Fig. 11f represents one of the most important results of this study and it would be interesting to see whether future laboratory and other natural scale geophysical flows find the same relationship between these parameters.

5. Insights from laboratory experiments and numerical simulations

There are numerous examples in the literature of experimental and numerical studies looking into the physical and dynamical processes of granular flows, with an aim to explain in particular the origin of the levee–channel morphology observed for some natural deposits (Félix and Thomas, 2004; Mangeney et al., 2007a; Kelfoun, 2011; Johnson et al., 2012). Existing experiments of self-channelling dry granular flows have been performed on constant slopes and can only be achieved on slopes around the repose angle of the material involved (Félix and Thomas, 2004). In these experiments, granular lobes of constant thickness are created by a constant supply applied upslope. During the flow, quasi-static zones develop naturally on the fringes of the flow, channelling the almost uniform central flow. When the supply of material to the flow stops, the material remaining within the channel drains to the front to form a frontal lobe. The channel is then of lower height than the levees. It is believed that the formation of levees results from the combination of lateral static zones on each border, inside of which is a central region where the velocity and thickness are almost uniform, and the drainage of the central part of the flow after the supply stops (Félix and Thomas, 2004; Mangeney et al., 2007a; Johnson et al., 2012).

Other studies have concentrated on the dynamics and kinematics of the flows and how this relates to depositional features once the flow has ceased. Notably, Pouliquen (1999b) found that a deposit of thickness h_{stop} remained on the slope after the supply of material was cut off which varied as a function of the slope angle for a given size of grain. The h_{stop} (θ) curve is found to be well described by

$$h_{stop}(\theta)/d_p = a/(\tan\theta - \tan\theta_1) \quad (4)$$

where d_p is the particle diameter, θ_1 is the vertical asymptote of the $h_{stop}(\theta)$ curve, corresponding to the (theoretical) minimum slope

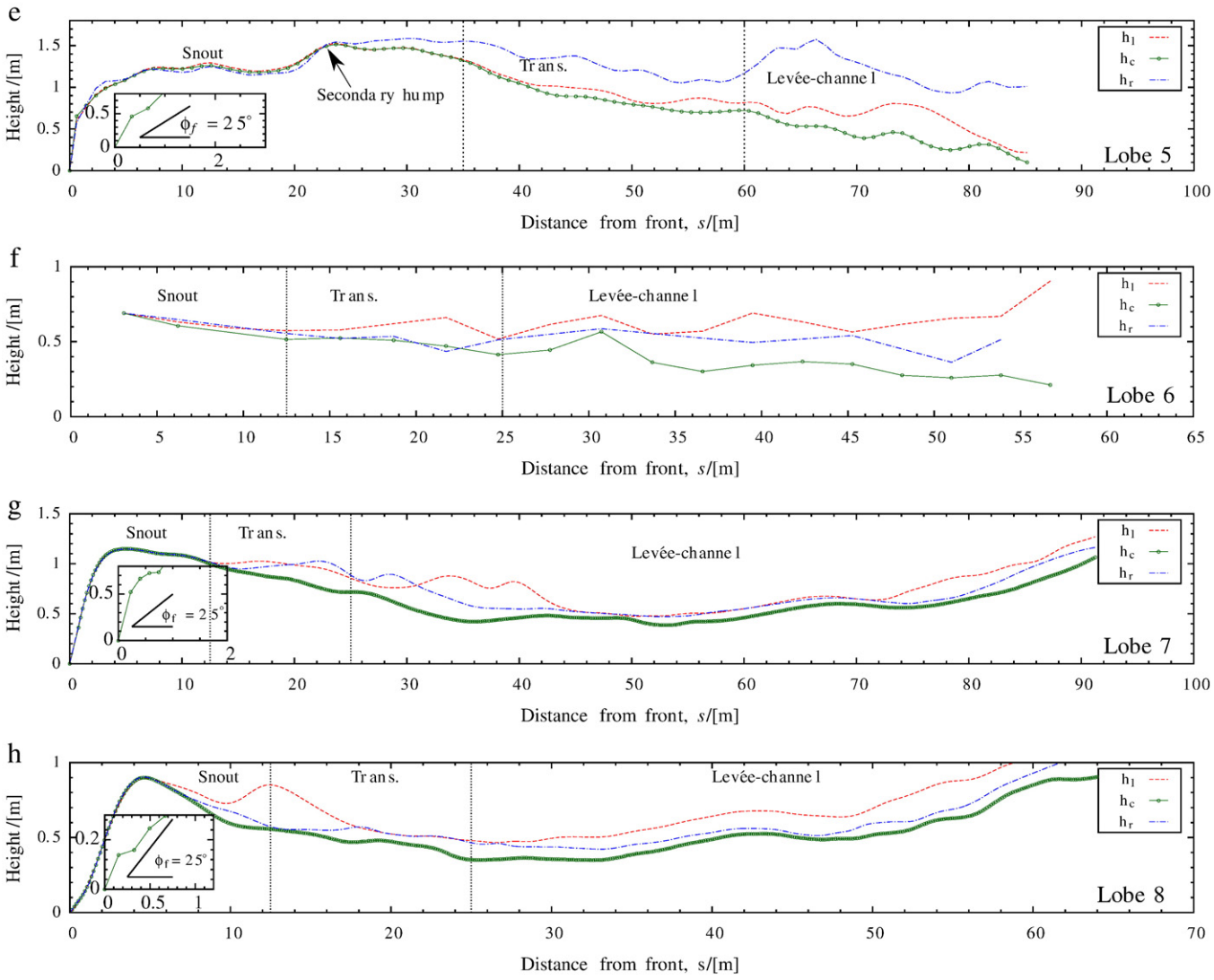

Fig. 8 (*continued*). Longitudinal height profiles of lobes 5 (e), 6 (f) (medial-east sector), and lobes 7 (g) and 8 (h) (distal sector).

angle for flow to occur and a is a dimensionless constant (Börzsönyi et al., 2008).

For these types of granular flow, a linear relationship is observed between the Froude number, $\mathrm{Fr} = u/\sqrt{gh}$ and the thickness of the flow, h, normalised with respect to the deposit thickness (e.g. Pouliquen and Forterre, 2002)

$$u/\sqrt{gh} = \beta h/h_{\mathrm{stop}} - \alpha \tag{5}$$

where β and α are dimensionless constants depending on the material and grain size, u is a characteristic speed of the flow and g the gravitational acceleration. Typical values for these constants are $\beta = 0.5$ and $\alpha = 0$ for glass beads (Félix and Thomas, 2004), $\beta = 0.65$ and $\alpha = 0.136$ for sand (Forterre and Pouliquen, 2003). Experimental results show that the flow thickness, h, and the mean levee height, h_{ave}, exhibit similar increase when the flux increases, so that $h/h_{levee} \equiv \gamma \simeq 1.25$ whatever the flux. As the polydispersivity of the material increases, γ increases up to 1.67, in the range of polydispersivity degree investigated by Félix and Thomas (2004).

The morphology of certain geophysical flow deposits has previously been used as a marker for the velocity when these flows encounter corners as they "slosh" towards the outside corner due to centrifugal effects (cf. section 1 of Fig. 6). Once the material in the central channel drains away, this leads to a difference in the heights of the deposit levees. This difference in height, h_{diff}, can be related to the velocity via

$$u = \sqrt{g h_{\mathrm{diff}} R/w} \tag{6}$$

where R is the radius of curvature of the corner and w the horizontal distance between the levees (Evans et al., 2001; Mangold et al., 2010). It should be noted that this expression comes about from a simple balance of gravitational and centripetal forces and neglects any rheological effects.

Particle segregation features, due to the migration of large particles towards the front and lateral borders of the flow, are common in geophysical flows, including coarse-grained pyroclastic flows (Pouliquen, 1999a; Félix and Thomas, 2004; Gray and Kokelaar, 2010; Wiederseiner et al., 2011; Johnson et al., 2012). The levee–channel morphology is reinforced (i.e. the difference between the levees and the channel is increased) for polydisperse mixtures although self-channelling and levees also spontaneously develop in monodisperse flows (Félix and Thomas, 2004; Mangeney et al., 2007a). Pouliquen and Vallance (1999) showed that for dry granular flows containing particles of several sizes and moving

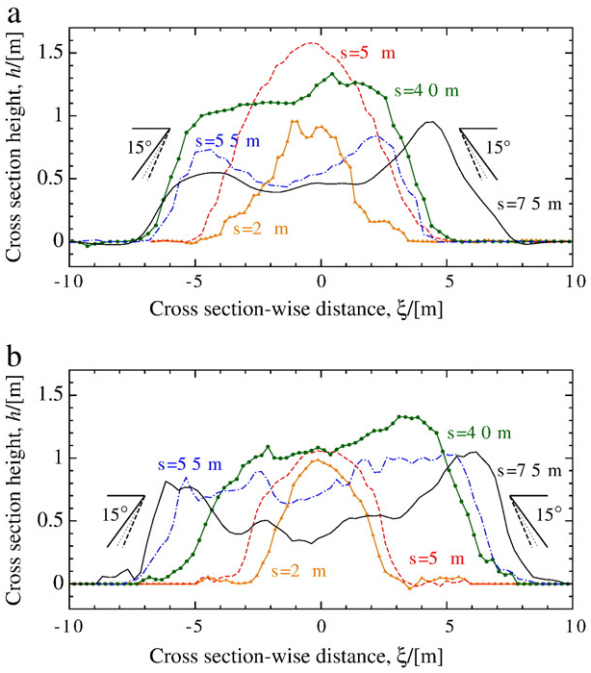

Fig. 9. Thickness profiles for various locations along the length of lobes (a) 2 and (b) 5 after the substratum has been removed from the deposit data. The sections in (a) correspond to those shown in Figs. 2 and 6. Note that the scale of the vertical axes is five-times larger than the scale of the horizontal axes. Slope indicators (15, 20 and 25°) show that the levee flanks have slope angles in this range.

down slopes, segregation of coarse-grained, irregularly shaped particles induces fingering instabilities at the propagating front that resemble the terminal part of some PDC deposits, in particular pumice flow lobes (see Rowley et al., 1981; Wilson and Head, 1981, for example). Fluidisation of granular flows can also enhance segregation of large particles to flow perimeters (e.g. Gilbertson and Eames, 2001), thus increasing permeability in the flow borders and making it possible to develop similar instabilities which owe their formation to the dry frictional perimeter that surrounds a partly fluidised interior.

Experimental and numerical studies of granular flows suggest that there are two types of morphological parameters: the first type is functions of the friction properties of the granular material and of the substratum, and is almost invariant with the flow dynamics. These parameters are (i) h_{stop} which represents the thickness left on a plane of inclination θ after the flow has passed (Pouliquen, 1999b; Pouliquen and Forterre, 2002) and is almost equal to the thickness of the central channel h_c for self-channelling flows (Félix and Thomas, 2004; Mangeney et al., 2007a), and (ii) the slope of the front at a given inclination θ (Pouliquen, 1999a). On the other hand, other morphological parameters vary as functions of the flow rate of material for a given slope angle, such as the thickness of the flow, h, the width of the central channel (Mangeney et al., 2007a) (approximately the same as the levee separation, w, in this study) and the total width of the flow, W. All these parameters are positively correlated with the slope angle.

By extracting various morphological parameters from field data (Table 1) and the use of dimensionless groups based on the morphological parameters (Table 2), we will qualitatively and, when possible, quantitatively compare our data to the experimental and numerical results recalled above.

6. Discussion

The previous section shows the variability of field data due, in particular, to the lobes studied consisting of multiple flow events, and local variations in slope angle. The variations in slope are generally small but are strong enough to significantly scatter the data.

We will try here to extract from these data the greatest possible amount of information that can be qualitatively compared to experimental and numerical modelling of granular flows. A significant difference between laboratory and field set up is that, for the former, each flow is generated on a constant slope, and the data are obtained by varying the slope angle and the rate of material release whereas, in nature, each flow occurs on a varying topography with unknown initial conditions. Few lobes makes it possible to investigate the variation of morphological parameters with slope, but notably lobe 7 experiences quasi-linear decrease of 4° in slope along its path (Fig. 7). This is however essential to keep in mind that the experimental granular flows are not only much simpler but also much smaller so that scale effects may be crucial, in particular when a fluid phase is involved (Iverson and Denlinger, 2001). Estimates of the dynamical and frictional properties are discussed based on differences and similarities between natural and experimental observations.

6.1. Frictional properties and emplacement processes

6.1.1. Qualitative features characteristic of granular flows

The general morphology of these lobes compares very well with experimental and numerical observations on granular flows over constant slope generated by a constant supply upslope: a rounded snout at the front progressively transforms upslope to a levee–channel morphology (see, for example, Figs. 4 and 6 of Félix and Thomas, 2004). As observed experimentally, the levees and the snout are made of bigger particles than the interior of the flow due to segregation processes (Pouliquen and Vallance, 1999; Félix and Thomas, 2004; Johnson et

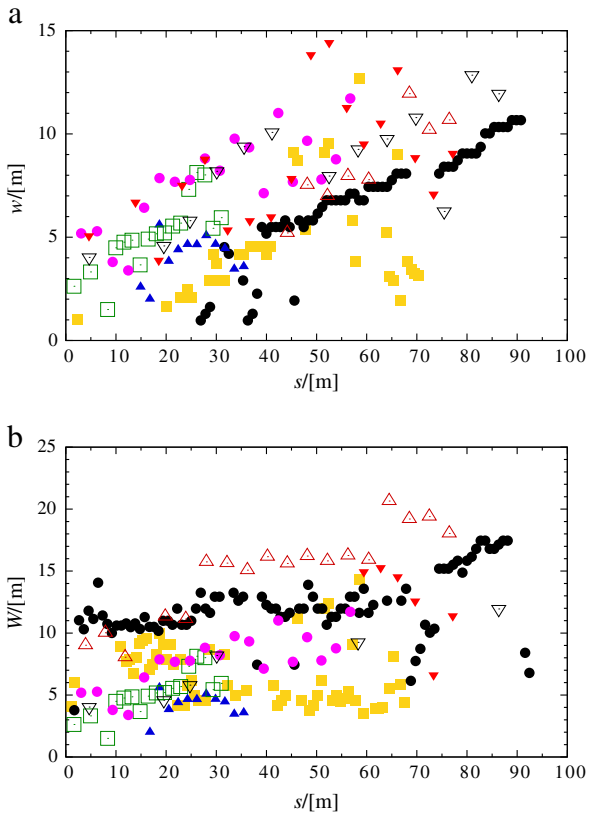

Fig. 10. Width of the lobes as a function of distance from the tip, s: (a) Separation of the levees, w, as a function of the distance from the tip, s; (b) the total width, W, as a function of s. The symbols used in both plots are for lobes: 1 (■), 2 (●), 3 (▲), 4 (□), 5 (△), 6 (◗), 7 (▽), 8 (▼). (For interpretation of the references to colour in this figure legend, the reader is referred to the web version of this article.)

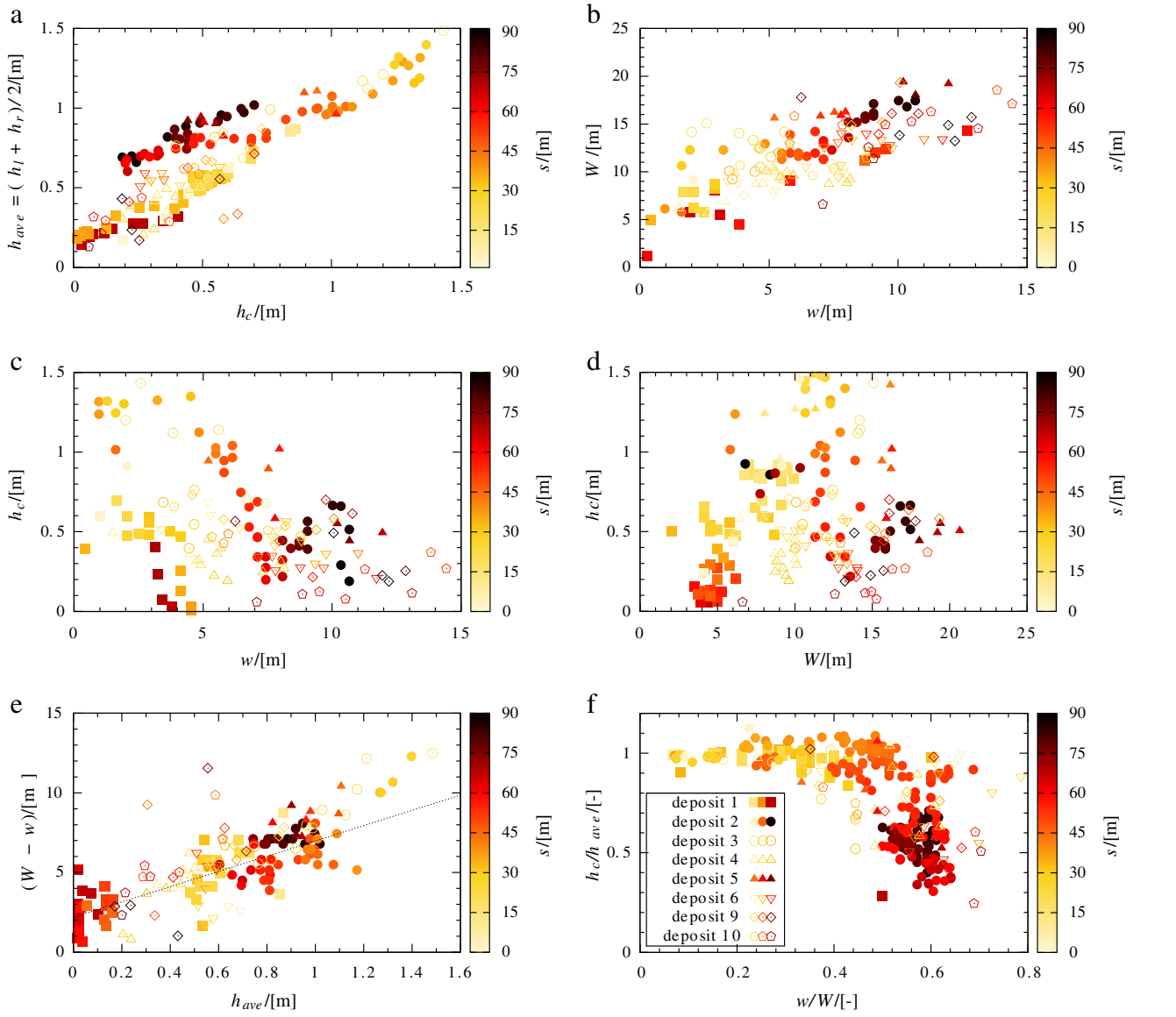

Fig. 11. Correlations between parameter groups for the pumice flow lobes. The tone of each data point indicates its distance from the front, *s*, according to the scale on the right-hand side. The data for lobes 1, 2 and 5 are plotted as solid symbols and the other lobes by open symbols, as per the key in (f): (a) The variation of the average levee thickness, h_{ave}, as a function of the thickness of middle of the central channel, h_c, for the levee–channel section of the lobes only. (b) The total width, *W*, of the lobe as a function of the levee width, *w*. The thickness of the central channel, h_c, as a function of the levee separation, *w* (c), and the total width, *W* (d). The parameters presented in these two plots are poorly correlated. (e) $W - w$ as a function of h_{ave}. A linear fit has been added (dotted line) of slope $4.86 \pm 0.40 (2\sigma)$ and intercept 2.11 ± 0.49. (f) The ratio of thicknesses, h_c/h_{ave}, as a function of the ratio of widths, w/W.

al., 2012). Furthermore, some particular features are very similar to small-scale experiments such as lobe-fingering instabilities which occur on the lateral borders of the flow (compare Fig. 15 of Félix and Thomas, 2004 and lobe 5 in Fig. 6) and, more generally, lobe generation at the distal regions of PDCs corresponds to finger-producing granular-front instabilities in polydisperse dry or fluidised granular flows over inclined planes (Pouliquen and Vallance, 1999).

6.1.2. Width of the lobes: competing slope and deposition processes

The total width of each lobe, *W*, is approximately constant or slightly increases with distance from the snout, *s*, for lobes lying on almost constant slopes in the levee–channel zone, except for the upper-most part where the lobe initiates. This zone is generally more complex as shown in Figs. 2 (e.g. lobe 2 and lobe 5 in Fig. 10b) and 6. For the other lobes the width, *W*, increases when moving away from the snout (i.e. towards higher slopes, e.g. lobes 6 and 7 on Fig. 10b). This is consistent with (i) the constant width or slightly increasing width observed experimentally and numerically for granular flows on constant slopes (Félix and Thomas, 2004; Mangeney et al., 2007a) and (ii) the linear increase of the width of experimental lobes as a function of the slope angle (e.g. Fig. 8 of Félix and Thomas, 2004). Experiments show that the width also increases almost linearly with the flux (Figs. 7 and 13 of Félix and Thomas, 2004). It may be then possible that further upslope, not only are slope angles larger but the flux may also be greater because of the deposition of material along the path. Deposition in laboratory-scale flows is compensated for by an imposed constant flux. Experimentally, an increase of 50% of the flux generates an increase of 20% of the width (Fig. 13a of Félix and Thomas, 2004). In the field data, taking lobes 4 and 5 which are situated on approximately equal slopes (8.5 and 9° respectively) a 30% increase in flux leads to a 40% increase in width. So one may expect that strong deposition occurred along lobe 7, for example, and that the supply (i.e. the flow upslope) was possibly decreasing with time. This supports the idea of multiple flow events of rather short duration, at least in the distal regions.

Table 1
Résumé of the data for comparing the morphological parameters for flows of different scales. Characteristic values for each of the pumice lobes have been taken; the experimental data for monodisperse and polydisperse flows are taken from Félix and Thomas (2004) (cf. their Fig. 17) and the simulation data are from Mangeney et al. (2007a). The grains used in the experiments of Félix and Thomas (2004) were approximately spherical glass beads with bulk density of approximately 1500 kg/m^3 for a volume fraction of about 0.6.

		Lobe snout			Channel		
		L/[m]	h_c/[m]	W/[m]	h_c/[m]	h_{ave}/[m]	w/[m]
Literature	Monodisperse	–	0.004	0.09	0.002	0.003	0.06
	Polydisperse	–	0.005	0.11	0.001	0.003	0.085
	Simulations	0.6	0.005	0.17	0.002	0.0027	0.11
This study	Pumice lobe 1	25	1	8	0.3	0.4	5
	Pumice lobe 2	35	1.8	10	0.5	0.9	6
	Pumice lobe 3	15	2	3	0.75	1	5
	Pumice lobe 4	6	0.75	4	0.3	0.5	5
	Pumice lobe 5	35	1.5	10	0.6	1	6
	Pumice lobe 6	12.5	0.6	5	0.3	0.6	10
	Pumice lobe 7	15	1.2	5	0.5	0.6	10
	Pumice lobe 8	15	0.9	5	0.5	0.6	5

Even though it is hard to interpret the width variation because of the competitive effects of slope and flux, the fact that $W\sim10$ m for lobe 1 and $W\sim15$ m for lobe 2, lying on almost the same slope, suggests that the initial flux was about 1.5 times larger for lobe 2. Lobe 5 has a larger width $W\sim16$ m although it is lying on a smaller slope, suggesting an even larger flux.

6.1.3. Proxies for the frictional properties and consequences for flow dynamics

Laterally-confined granular flows leave a deposit of thickness h_{stop} on the plane after the supply of material has been stopped, which is a characteristic of the slope angle and is well described by Eq. (4) (Pouliquen, 1999b; Pouliquen and Forterre, 2002; Börzsönyi et al., 2008). Laterally unconfined flows show the same behaviour for the channel thickness in the levee–channel zone after the supply ceases (Félix and Thomas, 2004). Lobe 7, due to the constant change in slope, is the best representation on the natural scale of the laboratory experiments. Fig. 12 shows a similar curve for the levee–channel section data of lobe 7 ($15\leq s\leq50$ m) where we have substituted h_c for h_{stop}, and fitted Eq. (4) to the data. Although the slope angles are much lower and the deposit thicknesses are larger than those found for laboratory-scale flows, the qualitative similarity between this plot and that seen in experiments is remarkable (see Fig. 9 of Félix and Thomas, 2004, for example). The $h_c(\theta)$ curve deduced from the data seems compatible with data in the levee–channel zone of other lobes suggesting that the frictional properties are similar in each case. Furthermore Fig. 12 shows that experimental observations, in which the height of the levees can be described by a curve of the form $h_{stop}(\theta)+C$ where C is a constant, seem to be borne out for the distal, self-channelling pumice lobes as $h_c(\theta)+C$ well describes the average levee thickness, h_{ave} (Félix and Thomas, 2004). From the data regression we deduce that the theoretical minimum slope angle is $\theta_1=5.73\pm0.002°$ (2σ). This suggests that the distal pumice flows would be unable to travel far over slopes of 6° or less as the frictional forces would be too great.

These small friction coefficients are consistent with the existence of lobes on very small slopes in the natural context. As a result the natural flow seems to experience much smaller friction than that of dry granular material. This may reflect the fluidisation of the granular material in pyroclastic flows widely discussed in the literature (Sparks, 1978; Wilson, 1980; Roche et al., 2004).

Figs. 6, 9 and 11e show that the slope of the external levee flanks do not change significantly along the lobes, ranging for all the lobes $\phi_{levee}\approx20$–$25°$, whereas the front angle with respect to the horizontal (i.e. taking into account the local slope angle and using the method shown in Appendix A) is $\phi_f+\theta\approx25$–$30°$ (see Table 2). It is known that the snout and levees of many types of polydisperse granular flows of all scales have roughly the same composition, consisting of much more coarse-grained material than the fines-rich interior of the flow (Félix and Thomas, 2004; Johnson et al., 2012). The slightly greater front angles may be an indicator that the dynamical processes that formed the front are slightly different to those that formed the flanks. In particular, if the flowing front suddenly came to a halt, the inertia of the material behind may have caused it to surge forward and overhang.

Experimental results give $\phi_{levee}\approx14°$ and $\phi_f+\theta\approx35°$ for polydisperse grains. The levee flank angles are vastly different between the two scales of flow which may be due to the large quantity of large, coarse-grained material in the pumice lobe flanks. It is interesting to note that the front angles of both scales of flow are similar, which may indicate that the dynamics are similar in the snout zone.

We have not made a detailed study of the *interior* levee slope angles, but we can see qualitatively from Figs. 6 and 9 that, at a constant angle of around 15°, these are substantially lower than the exterior levee flank angles discussed above. This would suggest that the core (i.e. central channel) of the flow propagated in a much more fluid-like manner. It has long been believed that fluidisation of the granular material by escaping gas plays an important role in the dynamics of PDCs, notably in enhancing their runout (Sparks, 1978; Wilson, 1980; Eames and Gilbertson, 2000; Roche et al., 2004). Fluidisation has the effect of reducing the internal friction angle and the angle of the deposit formed when the supply of material ceases. Hence a fluidised interior core would display lower interior levee flank angles. The levees, being composed of

Table 2
Dimensionless morphological parameters calculated for small- and large-scale flows. The slope angle and flux are approximately the same for the small-scale flows (25° and 7.1, 8 and 12 g/s respectively).

	Lobe snout		Channel			Angles			
	Long.	Lateral	Lateral	Height	Width	Flank	Front[a]	Slope	Combined
Definition	h_c/L	h_c/W	h_{ave}/w	h_c/h_{ave}	w/W	ϕ_{levee}/[°]	ϕ_f/[°]	θ/[°]	$\theta+\phi_f$/[°]
Monodisperse	–	0.044	0.05	0.67	0.67	11.3	7.89	~25	~35
Polydisperse	–	0.045	0.035	0.33	0.77	13.5	–	~25	–
Simulations	0.0045	0.025	0.018	0.75	0.64	5.1	~10	25	~35
Pumice lobe 1	0.040	0.13	0.08	0.75	0.63	14.93	13.36	9.5	22.86
Pumice lobe 2	0.050	0.18	0.15	0.56	0.6	24.23	20.41	8.5	28.91
Pumice lobe 3	0.133	0.67	0.89	0.75	0.71	–	–	10	–
Pumice lobe 4	0.125	0.19	0.625	0.6	0.83	–	–	8.5	–
Pumice lobe 5	0.043	0.15	0.25	0.6	0.6	26.57	18.85	9	27.85
Pumice lobe 6	0.048	0.12	0.4	0.5	0.67	–	–	7	–
Pumice lobe 7	0.08	0.24	0.06	0.83	0.83	18.63	20.92	6	26.92
Pumice lobe 8	0.06	0.18	0.09	0.83	0.69	19.04	21.85	7.5	29.35

[a] All front angles are measured relative to the substratum (according to the method indicated in A) so that the local slope angle must be added to find the front angle with respect to the horizontal.

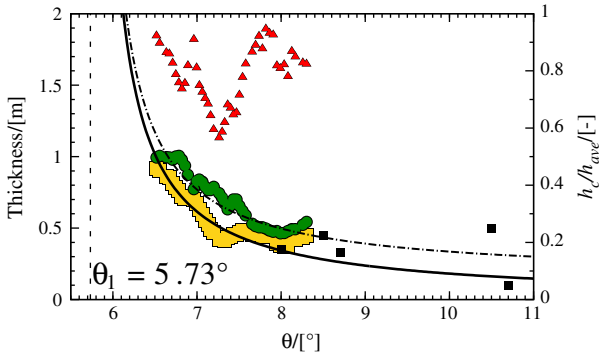

Fig. 12. Thickness of lobe 7 in the levee–channel zone ($15 \le s \le 50$ m) as a function of the slope angle. Shown are the channel thickness h_c ( ) and the fit according to Eq. (4) ( ) as well as the levee thickness ( ) and a fit of $h_c + C$ ( ), the h_c/h_{ave} ratio ( ) and the (theoretical) minimum slope angle for flow, $\theta_1 = 5.73°$. Whilst the fit for h_c has been performed solely with data from lobe 7, individual data points from other lobes are also plotted which are coherent with the data from lobe 7 (lobe 1: $h_c = 0.1$ m, $\theta = 10.7°$; lobe 2: 0.5 m, 10.5°; lobe 4: 0.33 m, 8.7°; lobe 6: 0.35 m, 8°; lobe 8: 0.45 m, 8.5°). (For interpretation of the references to colour in this figure legend, the reader is referred to the web version of this article.)

much coarser material of greater diffusivity, would defluidise much more rapidly and display greater flank angles.

6.2. Morphology as an indicator of flow processes

Different aspect ratios can be calculated using h_c, h_{ave}, w, W and L and are shown in Table 2. The aspect ratio h_c/W in the snout zone is found to be systematically an order of magnitude larger for PDCs than that obtained for numerical simulations and laboratory experiments. A similar trend is seen for the aspect ratio h_{ave}/w in the levee–channel zone although this is less robust, particularly for lobes 1, 7 and 8. On the other hand, the thickness ratio, h_c/h_{ave}, and the width ratio, w/W, in the levee–channel zone are approximately of the same order of magnitude in all cases. There are some distinct differences between the results for the small scale flows, notably between the monodisperse and polydisperse flows which were produced by a flux of almost exactly the same value. Therefore, part of the differences between the morphological parameters is probably due to polydispersivity effects (Félix and Thomas, 2004; Goujon et al., 2007).

6.2.1. Quantitative estimates of velocity and flux

Experimental and numerical simulations show an empirical relation between velocity and flowing thickness as given by Eq. (5). The deposit thickness in the experimental studies, h_{stop}, corresponds to the thickness of the central channel, h_c, in this study and the flowing thickness, $h = \gamma h_{ave}$, where γ is a constant of value 1.25 for monodisperse granular flows and 1.67 for polydisperse flows (Félix and Thomas, 2004; Mangeney et al., 2007a). Hence we may rewrite the Froude number defined by Eq. (5) as $u/\sqrt{g\gamma h_{ave}} = \beta\gamma h_{ave}/h_c - \alpha$. We assume that the values of $\beta = 0.65$ and $\alpha = 0.136$ found for sand may be approximately the same as would be found for the material in the pumice flows and that the value of γ found for polydisperse flows also holds for pumice flows. Using the information in Table 3, we see that α is approximately an order of magnitude smaller than $\beta\gamma h_{ave}/h_c$ so we chose to neglect it in the following analyses. As a result, the velocity can be estimated by

$$u \simeq \beta \frac{\sqrt{g\gamma^3 h_{ave}^3}}{h_c}. \tag{7}$$

Using some of the morphological data previously defined, the velocities and Froude numbers for the various scales of flows are calculated and presented in Table 3. There is of course a strong uncertainty in this velocity estimation related to both the empirical parameters in Eq. (7) and to the field measurements. The uncertainty can be roughly calculated as

$$\frac{\Delta u}{u} = \frac{\Delta\beta}{\beta} + \frac{3}{2}\left(\frac{\Delta\gamma}{\gamma} + \frac{\Delta h_{ave}}{h_{ave}}\right) + \frac{\Delta h_c}{h_c}. \tag{8}$$

The uncertainty on h_c and h_{ave} is the same and of the order of the uncertainty of the interpolation (see Section 3), so we take $\Delta h_c/h_c = \Delta h_{ave}/h_{ave} = 0.05$ and we assume that $\Delta\beta = 0.1$ and $\Delta\gamma = 0.15$. Thus, the relative uncertainty on the velocity is $\Delta u/u \simeq 0.496$ ($\simeq 50\%$), so that for lobe 2, $u = 7.50 \pm 3.72$ m/s. The velocity estimates for all the lobes are given in Table 3. Note that the estimated velocity of lobe 5 is very similar even though lobe 5 formed on shallower slopes. This is consistent with the wider width of lobe 5, presumably associated with higher flux as discussed in Section 6.1.2. It is not surprising that the velocities of lobe 7 and lobe 8 are found to be equal as these lobes originate from the same flow unit upslope and were flowing on similar slope angles. Alternatively, we may apply the formula in Eq. (6) to the morphological data when the pumice lobes are curved and the external levee more elevated than the internal levee. Taking lobe 6, for example, we find the approximate values: difference in heights of the levees, $h_{diff} \approx 0.5$ m, width, $w \approx 10$ m and radius of curvature, $R \approx 100$ m giving a velocity of $u \approx 7$ m/s. Clearly this is in agreement with the other velocity calculations.

The velocity estimates given in Table 3 correspond roughly with observations of pumice flows from other eruptions (Hobblit, 1986; Cole et al., 1998, 2002), where the velocity is of the order of 10 m/s. Again, we must recall that the lobes represent the stopping phase of the pumice flows where the deceleration is very large and that the velocity upslope would be greater. These estimates of the velocity can be used to approximate the flux of material within the central channel. Assuming that the flux is constant, a gross calculation is $Q_f \simeq uw\gamma h_{ave} = 40.5$ m^3/s for lobe 2 ($w = 6$ m). Flux estimations for this and the other lobes are given in Table 3. The error in determining the width is roughly equal to the error in determining the height, so $\Delta w/w = 0.05$. Therefore the uncertainty in estimating the flux is $\Delta Q/Q = 0.69$, or about 70%.

6.2.2. Dimensionless numbers

As h_c is representative of the frictional properties of the granular material and of the substratum, it appears as the most appropriate characteristic length scale of both natural and laboratory-scale systems. The ratio of characteristic lengths between experiments and field measurements is then defined as $L = h_c(\text{exp})/h_c(\text{field}) \simeq 10^{-3}$. The characteristic time of a flow is given by $\sqrt{h_c/g}$, so a ratio of characteristic times can be defined as $T = \sqrt{h_c(\text{exp})/h_c(field)} \simeq 10^{-2}$. Therefore the ratio of dimensionless fluxes can be approximated by $Q = L^3/T \simeq 10^{-7}$. Typical value for the flux in experiments is $Q(\text{exp}) = 1 \times 10^{-5}$ m^3/s and for the pumice flows we have $Q(\text{field}) = 20$ m^3/s. As the ratio $Q(\text{exp})/Q(\text{field}) \simeq 10^{-7} = O(Q)$, the suitability of h_c as a characteristic length scale is confirmed.

The important forces acting on the flows are inertia, gravity and friction from which we construct two dimensionless groups that determine the relative importance of these three forces. The first is the balance of inertia and gravity, which is the Froude number defined in Eq. (5). The second group balances the inertia against frictional (i.e. retarding) forces, the classic example being the Reynolds number which is the balance of inertial to viscous forces. As is shown in Appendix B, it is possible to construct a pseudo-Reynolds number for granular flows based on an effective viscosity. This is the viscosity required by a theoretical fluid subjected to the same shear rate to produce the same shear stresses. Doing this, we find the effective viscosity, η, to be in the order of 200 Pa·s, giving a pseudo-Reynolds number of

Table 3
Velocity and Froude number calculations for the flows of different scales according to Eqs. (5) and (7). The data is as per Table 1 with additional values from Félix and Thomas (2004) and Mangeney et al. (2007a). $\beta = 0.5$ for the experiments and simulations and 0.65 for the pumice lobes. $\gamma = 1.25$ for the monodisperse experiments and simulations and 1.67 for the polydisperse experiments and the pumice lobes.

	h_{ave}/[m]	h_c/[m]	h_{ave}/h_c	w/[m]	u[a]/[m/s]	$u/\sqrt{g\gamma h_{ave}}$	Q_f/[m^3/s]	Re/[–]
Monodisperse	0.003	0.002	1.5	–	0.18	0.94	–	0.5
Polydisperse	0.003	0.001	3.0	–	0.33	1.50	–	–
Simulations	0.0027	0.002	1.35	–	0.15	0.84	–	–
Pumice lobe 1	0.4	0.3	1.33	5	3.71	1.45	7.4	117
Pumice lobe 2	0.9	0.5	1.80	6	7.50	1.95	40.5	128
Pumice lobe 3	1.0	0.75	1.33	5	5.86	1.45	29.3	47
Pumice lobe 4	0.5	0.3	1.67	5	5.18	1.81	12.9	182
Pumice lobe 5	1.0	0.6	1.67	6	7.32	1.81	43.9	91
Pumice lobe 6	0.6	0.3	1.5	10	6.81	2.17	40.8	262
Pumice lobe 7	0.6	0.5	1.20	10	4.08	1.30	24.5	57
Pumice lobe 8	0.6	0.5	1.20	10	4.08	1.30	24.5	57

[a] Velocities calculated using Eq. (7). The flux, $Q_f \approx uwh_{ave}$ and the pseudo-Reynolds number, Re is defined in Appendix B.

about 100 for the pumice flow lobes whereas values of $\eta = 1.6$ Pa·s and Re = 0.5 are found for the (monodisperse) experimental flows.

Whilst the velocity of the flows on different scales is clearly very different, the Froude numbers, $u/\sqrt{g\gamma h_{ave}}$, shown in Table 3 are similar. The values for the calculated velocity are comparable with observations of other pumice flows, (e.g. the 1980 eruption of Mt. St. Helens, Levine and Kieffer, 1991). The Froude number for the polydisperse experimental flows was larger than the monodisperse case as the velocity was higher (certain polydisperse mixtures experience less resistance to flow due to the lubrication effect of the polydispersivity, Phillips et al., 2006; Goujon et al., 2007). Interestingly, the Froude numbers for the pumice flows are similar to the Froude number for both the polydisperse experiments and for laboratory experiments of initially fluidised powders (Roche et al., 2004, 2005), showing that the ratio of inertial and gravitational forces has not varied with the scale of the flow. However, as the calculations of Table 3 show, the inertia of the pumice flows relative to the retarding forces (given by the pseudo-Reynolds number, Re ≃ 100) is as much as two-hundred times larger for the pumice flows than for experimental scale flows. This finding can be interpreted as either (i) that the inertia of the pumice flows is large, or (ii) that the dissipation due to frictional forces is small compared with small-scale flows. In the former case, we would not expect to see the flows reacting quickly to changes in terrain, whereas there are many examples from the field study where the flow adapts to even the minutest change in slope. On the other hand, the relatively small dissipative mechanisms and hence enhanced mobility of pumice flows could be explained by one or a combination of several factors, as discussed below.

6.3. Interplay between different flowing zones

The overall picture of the pumice flow lobes is that of a central flow containing a large amount of finer particles flowing in between border zones and behind a frontal zone, made of bigger particles that behave as dry granular flows exhibiting higher friction than the central zone. This picture is very similar to the analysis of Pouliquen and Vallance (1999) where polydisperse fluidised granular flows exhibit fingering instabilities on small slopes. The decreased friction observed in the central part may be due to several processes as widely discussed in the literature (e.g. Legros, 2002; Lucas and Mangeney, 2007; Roche et al., 2011). It has been shown that the presence of an erodible bed can greatly enhance mobility of granular flows (Mangeney et al., 2007b, 2010). For slopes as gentle as 6°, however, entrainment of eroded material alone is insufficient to explain the observed increase in mobility. The high polydispersivity of the flow may also contribute to their mobility, and certain mixtures of particles size and/or shapes can greatly decrease the dissipation of energy within the flow through particles rolling over others (Roche et al., 2005; Phillips et al., 2006; Goujon et al., 2007). Recent work has indicated that the channelling effect of levee formation can enhance the run-out distance of granular flows (Gray and Kokelaar, 2010; Johnson et al., 2012). The increased mobility could also be partially explained by aeration/fluidisation of the material in the central channel that allows granular materials to flow like a fluid (Eames and Gilbertson, 2000; Roche et al., 2004, 2005; Jessop, 2009). When the fluidisation effect is insufficient to overcome frictional contacts within the granular material, the flows rapidly come to a halt (Roche et al., 2008, 2010). That for the pumice flows, the friction angles within the lateral borders and within the front are higher than within the central part (see Section 6.1) may suggest that these regions are defluidised. This is in keeping with observations of pumice flow emplacement and related phenomena, where the dynamics of the lateral borders of a flow may be significantly different from those of the main body as the lateral borders rapidly defluidise due to their higher permeability (Sparks, 1976; Iverson et al., 2010; Johnson et al., 2012). This process is very well described in Pouliquen and Vallance (1999) showing that for gas-fluidised flows, segregation processes drive big particles in the front zone and in the lateral borders of the flow, forming coarse-grained permeable perimeters that are dominated by Coulomb friction surrounding a fluidised fine-rich flow interior. As in nature, big particles are generally more angular, the friction coefficient in the front and lateral zone is higher than in the central part.

7. Concluding remarks

A study of the morphology of pumice flow deposits produced during the 1993 eruption of Lascar Volcano has been carried out using a LiDAR (laser scanning) device. The rheological properties of the pumice flows were inferred from the morphology of their deposits. The distal parts of pumice flow deposits (pumice lobes) can be separated into two distinct zones: a frontal snout and a levee–channel structure further upslope. These same features have been observed experimentally in the deposits left by self-channelling dense granular flows on slopes around the angle of repose (~30°). Hence it has been postulated that the dynamical processes that form these features are similar between the two scales, i.e. that the experiments performed on a laboratory scale are a suitable analogue for studying pumice flows in their terminal phases of deposition.

Using the data from our field measurements the variation of the pumice flow deposit morphology has been determined as a function of the distance from the front of the deposits. The slope angles of the underlying substratum have been estimated as a global trend as a function of the distance from the front. Several important correlations between morphological parameters have been identified. These include height/width aspect ratios of the snout and levee–channel section, the frontal and lateral angles formed by the deposits and the ratio of levee/channel height and levee separation/total width of the deposits. The height (h_c/h_{ave}) and width (w/W) ratios for the levee–channel zone of the pumice flows are almost identical to those seen in experimental and numerical studies. The h_c/W aspect ratio of the snout and hc/w aspect ratios in the

levee–channel section are larger by an order of magnitude in the field study than in small-scale flows. A key finding is that of the characteristic curve formed by plotting the ratio h_c/h_{ave} as a function of w/W, as shown in Fig. 11f. This is robustly observed for all the pumice lobes analysed.

For the sections of the deposits that were studied, the levee flank angle is approximately constant. Estimations of the lateral angles of the levees were deduced from the relationship between the levee separation to the mean levee height and also visually from the cross-sectional profiles. Both methods give levee flank angles of around 25°. This observation suggests that the composition of the levees is consistent along the length of the lobe deposits which may in turn suggest that the rheology of the flow that formed levees was locally constant during the depositional process.

Using the detailed information gathered on the morphology of pumice flows, combined with quantitative information on the dynamic and kinematic properties of the flowing material, it is possible to infer some rheological properties of the flowing material. We have been able to calculate a velocity and volume flow rate of the pumice flows. Estimates of the velocity are around 5–10 m/s which fits well with observed velocities of pumice flows from other eruptions, and we estimate a typical flow rate of 40 m^3/s. Using the velocity estimates, two key non-dimensional parameters that characterise the dynamics of granular flows (the Froude number and the pseudo-Reynolds number) have been calculated. The Froude numbers, Fr = 1.5–2, are almost identical for the pumice flows and laboratory scale experiments of polydisperse granular flows, which tells us that the velocity is scaled with the size of the flow. The pseudo-Reynolds number, Re ≃ 100, is found to be around two-hundred times larger for the pumice flows than for experimental-scale flows. The large pseudo-Reynolds number of the pumice flows suggests that the dissipative mechanisms that retard the flow (i.e. friction) are greatly reduced compared to flows on a small scale. This is further evidenced by the fact that pumice flows are able to travel large distances over terrain that has a much shallower slope (6–11°) than the angle of repose expected of granular materials (25–30°). It is possible that one or combination of mechanisms that include partial fluidisation of the central channel of the flow, erosion and entrainment of the underlying material, or "lubrication" due to the large range of particle sizes are responsible for the decrease in friction, although this remains an open question.

Acknowledgements

This is Laboratory of Excellence "ClerVolc" contribution no. 28 and LPGP contribution no. 3310. This study was funded through the ANR project VolBiFlo and with the financial support from INSU-PNTS. The authors wish also thank Electricité de France (EDF) for the technical support of the engineers of their Research and Development group, that installed and operated the Riegl LMS-Z420i 3D terrestrial scanner during the field survey. The authors would like to thank E. S. Calder and another anonymous reviewer for their insightful comments which have helped to improve our manuscript. This study was funded through the ANR project VolBiFlo.

Appendix A. Example of Taylor series expansions for calculating the front angle

Taylor series expansions allow functions near a point to be approximated for a given interval (see Stephenson, 1969, for example). These take the form

$$h(x) = h(a) + (x-a)h'(a) + (x-a)^2/2!h''(a) + \ldots,$$

for a given interval $a<x<b$ and where a prime denotes differentiation with respect to x. Taking h to be the thickness of a flow and putting this into a discrete form we then may write $h_j = h(x_j)$ and hence

$$h_j = h_1 + (j\Delta x)h_1' + (j\Delta x)^2/2!h_1'' + \ldots, \quad (A1)$$

for a point $x_j = x_1 + j\Delta x$. The same may be done for successive points x_2, x_3, x_4, x_5 and the results summed in such a way that the terms in h_1'' are eliminated. What remains is an estimate for the gradient at x_1, h_1'

$$h_1' = -1/2(h_1 + h_2 - 2h_3 - h_4 + h_5)/\Delta x, \quad (A2)$$

where the truncation error is of $O(\Delta x)^2$. The front angle is hence, $\phi_f = \mathrm{atan}(h_1')$. Calculations for "noisy" data using this method tend to be more reliable than a simple two-point calculation as there are more data points used.

Appendix B. Calculation of effective viscosity and Reynolds number

The continuum hypothesis is generally believed to hold for granular media as long as the important length scales for mechanical processes, e.g. shear, are much greater than the particle size (see Drew, 1983, for example). Under this assumption, it is reasonable to think of flows of granular media as having fluid-like properties, such as viscosity. Jop et al. (2006) suggested that, if the granular flow could be considered as a viscous fluid under the same conditions of shear stress and shear rate, an effective viscosity could be written as

$$\eta(\dot{\gamma}, p) = \mu(I)p/\dot{\gamma}, \quad (B1)$$

where $\dot{\gamma}$ is the shear rate, $\mu(I)$ is the coefficient of friction that depends on the inertia number, $I = \dot{\gamma}d_p/\sqrt{p/\rho_s}$, ρ_s is the density of the solid material and d_p is the particle diameter. The above relationship can readily be devised by comparing Eqs. (1) and (3) of Jop et al. (2006). We will assume that the pressure distribution is hydrostatic so that for a height, h, and bulk density, ρ, the pressure is given by $p = \rho g h$ and that the shear rate can be approximated by $\dot{\gamma} = u/h$ for a flow characteristic speed of u.

An important parameter for the comparison of flows on different scales and of different materials is the Reynolds number, $\mathrm{Re} = \rho u h/\eta$, with ρ as the bulk density of the pumice flow, which compares the relative importance of inertia and "viscous" effects. Note that the bulk density depends on the volume fraction and density of pumices (~800 kg/m^3), and will be less than the bulk density of the ash matrix (~1500 kg/m^3). Furthermore, the granular flow regime can be estimated by the inertial number from the quasi-static to the collisional (Campbell, 2006; Forterre and Pouliquen, 2008). We will now attempt to calculate the relevant parameters for a laboratory-scale flow, using data from Félix and Thomas (2004) and pumice flows using our own data. There is uncertainty over the value we find for u, as found in Section 1, as we are obliged to estimate many parameters based on comparisons with experimental and numerical data. However, the values of 5–10 m/s compare well with the observed velocity of pumice flows on Montserrat (Druitt, 1998) and is of the same order of magnitude as the 7th August 1986 pyroclastic flows at Mount St. Helens (Hobblit, 1986). For ease of comparison we present this in a tabular form in Table B1.

Values of I much less than 0.1 are typically quasi-static whereas collisional stresses become more important when this parameter becomes larger (Campbell, 2006). It is not a simple matter to make an estimate of the inertia number for the pumice flows because we do not have good constraints on the characteristic particle diameter. Furthermore, it is not clear that even with a well-defined characteristic particle size that the resulting inertial number is then characteristic

Table B1
Magnitudes of parameters for the calculation of the inertial number, I, effective viscosity, η, and Reynolds number, Re. Values for the experimental data are all taken from Félix and Thomas (2004) whilst the pumice flow data is based on our measurements† and educated guesses‡ or else are derived from other values (see text for details). We take the height of the frontal snout of the pumice flow lobes to be a proxy for the height of the flow in motion.

	Experiment	Pumice flow
ρ/[kg/m^3]	1500	1000†
ρ_s/[kg/m^3]	2500	2500‡
d_p/[m]	5×10^{-4}	0.01 to 0.1†
u/[m/s]	0.1	5†
h/[m]	0.005	1†
g/[m/s^2]	9.81	9.81
p/[Pa]	75	10,000
$\dot{\gamma}$/[1/s]	20	5
I/[−]	0.058	0.02 to 0.2
θ_s/[°]	23	5.73†
$\mu(I\rightarrow0)$/[−]	0.425	0.1‡
η/[Pa·s]	1.562	200
Re/[−]	0.480	25

for the flow. The friction coefficient varies as a function of the inertia number between the critical value $\mu_s=\tan(\theta_s)$ at zero shear rate and converges asymptotically to μ_2 at high values of I, i.e. very large shear rates (Jop et al., 2006). The critical angle can be determined from Félix and Thomas (2004) to be $\theta_s\approx23°$ so that for low shear, $\mu(I\rightarrow0)\approx\mu_s=\tan\theta_s=0.425$. For the pumice flows, we have found that the minimum slope angle for lobe 7 was around 6°, so the friction coefficient will be lower than for the experiments. We estimate $\mu=\tan(6°)\approx0.1$. Therefore, using Eq. (B1) we may calculate the remaining parameters that are given in Table B1.

Of course, there are a great number of parameters whose values have been estimated or assumed, and as many which have a large uncertainty over their value. The values chosen for all the parameters are representative of the order of magnitude so that these calculations show, at least to an order of magnitude, that the role of inertia relative to retarding forces is much more important in the natural-scale flows as compared to laboratory-scale flows.

References

Ackermann, F., 1999. Airborne laser scanning—present status and future expectations. ISPRS Journal of Photogrammetry and Remote Sensing 54 (2–3), 64–67.

Ancey, C., 2007. Plasticity and geophysical flows: a review. Journal of Non-Newtonian Fluid Mechanics 142, 4–35.

Baltsavias, E.P., 1999. A comparison between photogrammetry and laser scanning. ISPRS Journal of Photogrammetry and Remote Sensing 54 (2–3), 83–94.

Bellian, J., Kerans, C., Jennette, D., 2005. Digital outcrop models: applications of terrestrial scanning LiDAR technology in stratigraphic modeling. Journal of Sedimentary Research 75 (2), 166–176.

Börzsönyi, T., Halsey, T.C., Ecke, R.E., 2008. Avalanche dynamics on a rough inclined plane. Physical Review E 78, 011306.

Branney, M.J., Kokelaar, B.P., 1992. A reappraisal of ignimbrite emplacement—progressive aggradation and changes from particulate to nonparticulate flow during emplacement of high-grade ignimbrite. Bulletin of Volcanology 54 (6), 504–520.

Calder, E.S., Cole, P.D., Dade, W.B., Druitt, T.H., Hoblitt, R.P., Huppert, H.E., Ritchie, L., Sparks, R.S.J., Young, S.R., 1999. Mobility of pyroclastic flows and surges at the Soufrière Hills Volcano, Montserrat. Geophysical Research Letters 26 (5), 537–540.

Calder, E.S., Sparks, R.S.J., Gardeweg, M.C., 2000. Erosion, transport and segregation of pumice and lithic clasts in pyroclastic flows inferred from ignimbrite at Lascar Volcano, Chile. Journal of Volcanology and Geothermal Research 104, 201–235.

Campbell, C.S., 2006. Granular material flows—an overview. Powder Technology 126, 208–209.

Cassidy, N.J., Calder, E.S., Pavez, A., Wooller, L., 2009. Gpr-derived facies architectures: a new perspective on mapping pyroclastic flow deposits. In: Thordarson, T., Self, S., Larsen, G., Rowland, S., Hoskuldsson, A. (Eds.), Studies in Volcanology: The Legacy of George Walker. Geological Soc. Publishing House, pp. 181–210.

Choux, C., Druitt, T., 2002. Analogue study of particle segregation in pyroclastic density currents, with implications for the emplacement mechanisms of large ignimbrites. Sedimentology 49 (5), 907–928.

Cole, P.D., Calder, E.S., Druitt, T.H., Hoblitt, R., Robertson, R., Sparks, R.S.J., Young, S.R., 1998. Pyroclastic flows generated by gravitational instability of the 1996–97 lava dome of Soufrière Hills Volcano, Montserrat. Geophysical Research Letters 25 (18), 3425–3428.

Cole, P.D., Calder, E.S., Sparks, R.S.J., Clarke, A.B., Druitt, T.H., Young, S.R., Herd, R.A., Harford, C.L., Norton, G.E., 2002. Deposits from dome-collapse and fountain-collapse pyroclastic flows at Soufrière Hills Volcano, Montserrat. The Eruption of Soufrière Hills Volcano, Montserrat, from 1995 to 1999: Geol. Soc, Lond. Mem., vol. 21, pp. 231–262.

Doyle, E.E., Hogg, A.J., Mader, H.M., Sparks, R.S.J., 2008. Modeling dense pyroclastic basal flows from collapsing columns. Geophysical Research Letters 35 (4).

Drew, D.A., 1983. Mathematical modeling of two-phase flow. Annual Review of Fluid Mechanics 15, 261–291.

Druitt, T.H., 1998. Pyroclastic density currents. In: Gilbert, J., Sparks, R.S.J. (Eds.), The Physics of Explosive Volcanic Eruptions: Geol. Soc. Spec. Publ., London, vol. 145, pp. 145–182.

Druitt, T., Calder, E., Cole, P., Hoblitt, R., Loughlin, S., Norton, G., Ritchie, L., Sparks, R., Voight, B., 2002. Small-volume, highly mobile pyroclastic flows formed by rapid sedimentation from pyroclastic surges at Soufrière Hills Volcano, Montserrat: an important volcanic hazard. In: Druitt, T., Kokelaar, B. (Eds.), The Eruption of Soufrière Hills Volcano, Montserrat, from 1995 to 1999. Geological Soc. Publishing House, pp. 263–279.

Eames, I., Gilbertson, M.A., 2000. The flow of aerated particles over a horizontal rigid surface. Journal of Fluid Mechanics 424, 169–195.

Evans, S.G., Hungr, O., Clague, J.J., 2001. Dynamics of the 1984 rock avalanche and associated distal debris flow on Mount Cayley, British Columbia, Canada; implications for landslide hazard assessment on dissected volcanoes. Engineering Geology 61 (1), 29–51.

Favreau, P., Mangeney, A., Lucas, A., Crosta, G., Bouchut, F., 2010. Numerical modeling of landquakes. Geophysical Research Letters 37.

Félix, G., Thomas, N., 2004. Relation between dry granular flow regimes and morphology of deposits: formation of levées in pyroclastic deposits. Earth and Planetary Science Letters 197–213.

Forterre, Y., Pouliquen, O., 2003. Long-surface-wave instability in dense granular flows. Journal of Fluid Mechanics 486, 21–50.

Forterre, Y., Pouliquen, O., 2008. Flows of dense granular media. Annual Review of Fluid Mechanics 40, 1–24.

Fox, J., 1997. Applied Regression Analysis, Linear Models, and Related Methods. Sage.

Francis, P., Rothery, D., 1987. Using the Landsat Thematic Mapper to detect and monitor active volcanoes: an example from Lascar Volcano, northern Chile. Geology 15 (7), 614–617.

Gardeweg, M.C., Sparks, R.S.J., Matthews, S.J., 1998. Evolution of Lascar Volcano, northern Chile. Journal of the Geological Society 155 (1), 89–104.

Gilbertson, M.A., Eames, I., 2001. Segregation patterns in gas-fluidized systems. Journal of Fluid Mechanics 433, 347–356.

Goujon, C., Dalloz-Dubrujeaud, B., Thomas, N., 2007. Bidisperse granular avalanches on inclined planes: a rich variety of behaviors. The European Physical Journal. E, Soft Matter 23 (2), 199–215.

Gray, J.M.N.T., Kokelaar, B.P., 2010. Large particle segregation, transport and accumulation in granular free-surface flows. Journal of Fluid Mechanics 657, 539.

Hibert, C., Mangeney, A., Grandjean, G., Shapiro, N.M., 2011. Slope instabilities in Dolomieu crater, Reunion Island: from seismic signals to rockfall characteristics. Journal of Geophysical Research, Solid Earth 116.

Hobblit, R.P., 1986. Observations of the eruptions of 22 July and 7 August 1986, at Mount St. Helens, Washington. U.S. Geological Survey, Professional Paper, 1335.

Hulme, G., 1974. Interpretation of lava flow morphology. Geophysical Journal of the Royal Astronomical Society 39 (2), 361–383.

Iverson, R.M., 1997. The physics of debris flows. Reviews of Geophysics 35 (3), 245–296.

Iverson, R., Denlinger, R., 2001. Flow of variably fluidized granular masses across three-dimensional terrain 1. Coulomb mixture theory. Journal of Geophysical Research, Solid Earth 106 (B1), 537–552.

Iverson, R.M., Logan, M., LaHusen, R.G., Berti, M., 2010. The perfect debris flow? Aggregated results from 28 large-scale experiments. Journal of Geophysical Research, Solid Earth 115.

James, M.R., Pinkerton, H., Applegarth, L.J., 2009. Detecting the development of active lava flow fields with a very-long-range terrestrial laser scanner and thermal imagery. Geophysical Research Letters 36.

Jessop, D.E. 2009, *On flows of fluidised particles down slopes*, PhD thesis, Department of Mathematics, University of Bristol.

Johnson, C.G., Kokelaar, B.P., Iverson, R.M., Logan, M., LaHusen, R.G., Gray, J.M.N.T., 2012. Grain-size segregation and levee formation in geophysical mass flows. Journal of Geophysical Research, Solid Earth 117, F01032.

Jones, R.R., Kokkalas, S., McCaffrey, K.J.W., 2009. Quantitative analysis and visualization of nonplanar fault surfaces using terrestrial laser scanning (LIDAR)—the Arkitsa fault, central Greece, as a case study. Geosphere 5 (6), 465–482.

Jop, P., Forterre, Y., Pouliquen, O., 2006. A constitutive law for dense granular flows. Nature 441 (8), 727–730.

Kelfoun, K., 2011. Suitability of simple rheological laws for the numerical simulation of dense pyroclastic flows and long-runout volcanic avalanches. Journal of Geophysical Research, Solid Earth 116.

Kern, M., Tiefenbacher, F., McElwaine, J., 2004. The rheology of snow in large chute flows. Cold Regions Science and Technology 39 (2–3), 181–192.

Legros, F., 2002. The mobility of long-runout landslides. Engineering Geology 63 (3–4), 301–331.

Levine, A., Kieffer, S., 1991. Hydraulics of the August 7, 1980, pyroclastic flow at Mount St. Helens, Washington. Geology 19 (11), 1121–1124.

Lube, G., Cronin, S.J., Platz, T., Freundt, A., Procter, J.N., Henderson, C., Sheridan, M.F., 2007. Flow and deposition of pyroclastic granular flows: a type example from the 1975

Ngauruhoe eruption, New Zealand. Journal of Volcanology and Geothermal Research 161 (3), 165–186.
Lucas, A., Mangeney, A., 2007. Mobility and topographic effects for large Valles Marineris landslides on Mars. Geophysical Research Letters 34 (10), L10201.
Ma, R., 2005. DEM generation and building detection from LiDAR data. Photogrammetric Engineering and Remote Sensing 71 (7), 847–854.
Mangeney, A., 2011. Landslide boost from entrainment. Nature Geoscience 4 (2), 77–78.
Mangeney, A., Bouchut, F., Thomas, N., Vilotte, J.P., Bristeau, M.O., 2007a. Numerical modeling of self-channelling granular flows and of their levée channel deposits. Journal of Geophysical Research, Solid Earth 112, F02017.
Mangeney, A., Tsimring, L.S., Volfson, D., Aranson, I.S., Bouchut, F., 2007b. Avalanche mobility induced by the presence of an erodible bed and associated entrainment. Geophysical Research Letters 34.
Mangeney, A., Roche, O., Hungr, O., Mangold, N., Faccanoni, G., Lucas, A., 2010. Erosion and mobility in granular collapse over sloping beds. Journal of Geophysical Research, Solid Earth 115, F03040.
Mangold, N., Mangeney, A., Migeon, V., Ansan, V., Lucas, A., Baratoux, D., Bouchut, F., 2010. Sinuous gullies on Mars: frequency, distribution, and implications for flow properties. Journal of Geophysical Research, Solid Earth 115, E11001.
Matthews, S.J., Gardeweg, M.C., Sparks, R.S.J., 1997. The 1984 to 1996 cyclic activity of Lascar Volcano, northern Chile: cycles of dome growth, dome subsidence, degassing and explosive eruptions. Bulletin of Volcanology 59 (1), 72–82.
Pavez, A., Remy, D., Bonvalot, S., Diament, M., Gabalda, G., Froger, J.-L., Julien, P., Legrand, D., Moisset, D., 2006. Insight into ground deformations at Lascar Volcano (Chile) from SAR interferometry, photogrammetry and GPS data: implications on volcano dynamics and future space monitoring. Remote Sensing of Environment 100 (3), 307–320.
Phillips, J., Hogg, A., Kerswell, R., Thomas, N., 2006. Enhanced mobility of granular mixtures of fine and coarse particles. Earth and Planetary Science Letters 246 (3–4), 466–480.
Pouliquen, O., 1999a. On the shape of granular fronts down rough inclined planes. Physics of Fluids 11 (7), 1956–1958.
Pouliquen, O., 1999b. Scaling laws in granular flows down rough inclined planes. Physics of Fluids 11 (3), 542–548.
Pouliquen, O., Forterre, Y., 2002. Friction law for dense granular flows: application to the motion of a mass down a rough inclined plane. Journal of Fluid Mechanics 453, 133–151.
Pouliquen, O., Vallance, J., 1999. Segregation induced instabilities of granular fronts. Chaos 9 (3), 621–630.
Pyle, D.M., Elliott, J.R., 2006. Quantitative morphology, recent evolution, and future activity of the Kameni Islands Volcano, Santorini, Greece. Geosphere 2 (5), 253–268.
Roche, O., Gilbertson, M.A., Phillips, J.C., Sparks, R.S.J., 2002. Experiments on deaerating granular flows and implications for pyroclastic flow mobility. Geophysical Research Letters 29 (16).
Roche, O., Gilbertson, M.A., Phillips, J.C., Sparks, R.S.J., 2004. Experimental study of gas-fluidized granular flows with implications for pyroclastic flow emplacement. Journal of Geophysical Research, Solid Earth 109.
Roche, O., Gilbertson, M.A., Phillips, J.C., Sparks, R.S.J., 2005. Inviscid behaviour of fines-rich pyroclastic flows inferred from experiments on gas–particle mixtures. Earth and Planetary Science Letters 240, 401–414.
Roche, O., Montserrat, S., Niño, Y., Tamburrino, A., 2008. Experimental observations of water-like behaviour or initially fluidized, unsteady dense granular flows and their relevance for the propagation of pyroclastic flows. Journal of Geophysical Research, Solid Earth 113, B12103.
Roche, O., Montserrat, S., Niño, Y., Tamburrino, A., 2010. Pore fluid pressure and internal kinematics of gravitational laboratory air–particle flows: insights into the emplacement dynamics of pyroclastic flows. Journal of Geophysical Research, Solid Earth 115, B09206.
Roche, O., Attali, M., Mangeney, A., Lucas, A., 2011. On the run-out distance of geophysical gravitational flows: insight from fluidized granular collapse experiments. Earth and Planetary Science Letters 311 (34), 375–385.
Rowley, P.D., Kuntz, M.A., McLeod, N.S., 1981. Pyroclastic flow deposit. In: Lipman, P.W., Mullineaux, D.R. (Eds.), The 1980 Eruption of Mount St. Helens, Washington. US Geol. Prof. Paper 1250, vol. 1250. University of Washington Press, pp. 489–512.
Smithsonian Institution, 1993. Lascar. Bulletin of the Global Volcanism Network 18 (11), 11–12.
Sparks, R.S.J., 1976. Grain-size variations in ignimbrites and implications for transport of pyroclastic flows. Sedimentology 23 (2), 147–188.
Sparks, R.S.J., 1978. Gas release rates from pyroclastic flows: an assessment of the role of fluidisation in their emplacement. Bulletin of Volcanology 41 (1), 1–9.
Sparks, R.S.J., Gardeweg, M.S., Calder, E.S., Matthews, S.J., 1997. Erosion by pyroclastic flows on Lascar Volcano, Chile. Bulletin of Volcanology 58 (7), 557–565.
Stephenson, G., 1969. Mathematical Methods for Science Students. Longmans.
Whelley, P., Jay, J., Calder, E., Pritchard, M., Cassidy, N., Alcaraz, S., Pavez, A., 2011. Post-depositional fracturing and subsidence of pumice flow deposits: Lascar Volcano, Chile. Bulletin of Volcanology 1–21.
Wiederseiner, S., Andreini, N., Epely-Chauvin, G., Moser, G., Monnereau, M., Gray, J.M.N.T., Ancey, C., 2011. Experimental investigation into segregating granular flows down chutes. Physics of Fluids 23 (1).
Wilson, C.J.N., 1980. The role of fluidization in the emplacement of pyroclastic flows: an experimental approach. Journal of Volcanology and Geothermal Research 8, 231–249.
Wilson, L., Head, J.W., 1981. Morphology and rheology of pyroclastic flows and their deposits, and guidelines for future observations. In: Lipman, P.W., Mullineaux, D.R. (Eds.), The 1980 Eruption of Mount St. Helens, Washington. US Geol. Prof. Paper 1250, vol. 1250. University of Washington Press, pp. 513–524.